



Observation of $J/\psi p$ resonances consistent with pentaquark states in $\Lambda_b^0 \rightarrow J/\psi K^- p$ decays

The LHCb collaboration¹

Abstract

Observations of exotic structures in the $J/\psi p$ channel, that we refer to as pentaquark-charmonium states, in $\Lambda_b^0 \rightarrow J/\psi K^- p$ decays are presented. The data sample corresponds to an integrated luminosity of 3 fb^{-1} acquired with the LHCb detector from 7 and 8 TeV pp collisions. An amplitude analysis is performed on the three-body final-state that reproduces the two-body mass and angular distributions. To obtain a satisfactory fit of the structures seen in the $J/\psi p$ mass spectrum, it is necessary to include two Breit-Wigner amplitudes that each describe a resonant state. The significance of each of these resonances is more than 9 standard deviations. One has a mass of $4380 \pm 8 \pm 29 \text{ MeV}$ and a width of $205 \pm 18 \pm 86 \text{ MeV}$, while the second is narrower, with a mass of $4449.8 \pm 1.7 \pm 2.5 \text{ MeV}$ and a width of $39 \pm 5 \pm 19 \text{ MeV}$. The preferred J^P assignments are of opposite parity, with one state having spin $3/2$ and the other $5/2$.

Submitted to Phys. Rev. Lett.

© CERN on behalf of the LHCb collaboration, license CC-BY-4.0.

¹Authors are listed at the end of this Letter.

Executive summary

The prospect of hadrons with more than the minimal quark content ($q\bar{q}$ or qqq) was proposed by Gell-Mann in 1964 [1], followed by a quantitative model for two quarks plus two antiquarks developed by Jaffe in 1976 [2]. The idea was expanded upon by Strottman in 1979 [3] to include baryons composed of four quarks plus one antiquark; the name pentaquark was coined by Lipkin [4]. Past claimed observations of pentaquark states have been shown to be spurious [5], although there is at least one viable tetraquark candidate, the $Z(4430)^+$ that has been observed in $\bar{B}^0 \rightarrow \psi' K^- \pi^+$ decays [6–8], implying that the existence of pentaquark baryon states would not be surprising. States that decay into charmonium may have particularly distinctive signatures [9].

Large yields of $\Lambda_b^0 \rightarrow J/\psi K^- p$ decays are available at LHCb and have been used for the precise measurement of the Λ_b^0 lifetime [10]. (In this Letter mention of a particular mode implies use of its charge conjugate as well.) This decay can proceed by the diagram shown in Fig. 1(a), and is expected to be dominated by Λ^* resonances, as are evident in our data shown in Fig. 2(a). It could also have exotic contributions, as indicated by the diagram in Fig. 1(b), that could result in resonant structures in the $J/\psi p$ mass spectrum shown in Fig. 2(b).

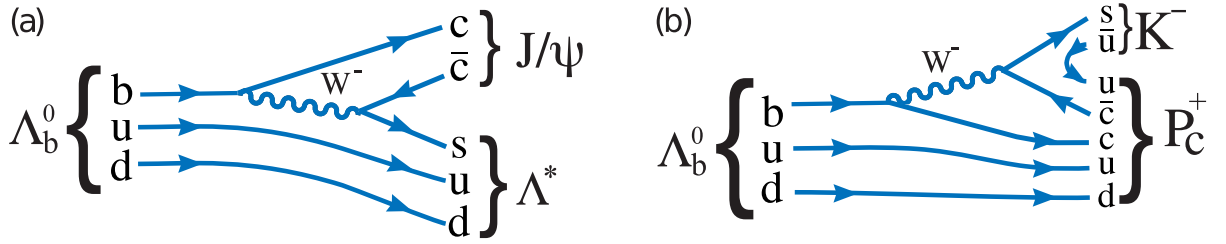


Figure 1: Feynman diagrams for (a) $\Lambda_b^0 \rightarrow J/\psi \Lambda^*$ and (b) $\Lambda_b^0 \rightarrow P_c^+ K^-$ decay.

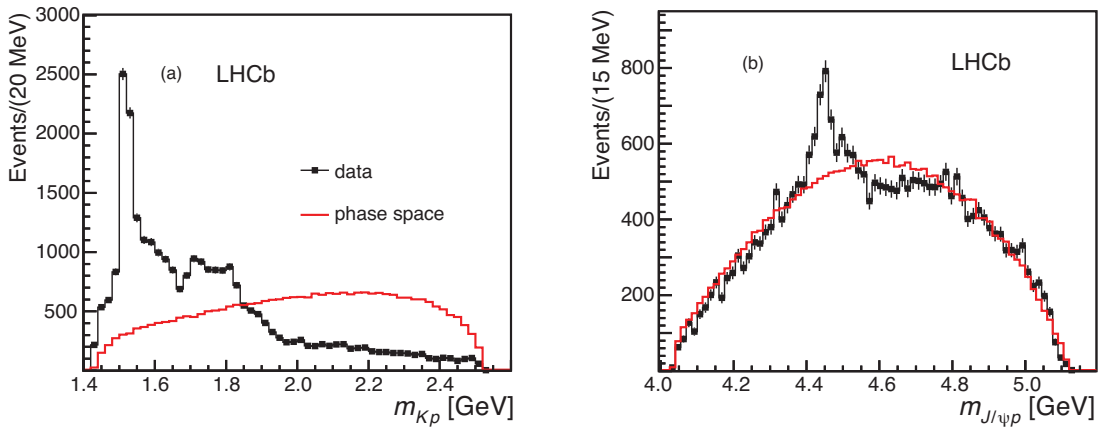


Figure 2: Invariant mass of (a) $K^- p$ and (b) $J/\psi p$ combinations from $\Lambda_b^0 \rightarrow J/\psi K^- p$ decays. The solid (red) curve is the expectation from phase space. The background has been subtracted.

In practice resonances decaying strongly into $J/\psi p$ must have a minimal quark content of $c\bar{c}uud$, and thus are charmonium-pentaquarks; we label such states P_c^+ , irrespective of the internal binding mechanism. In order to ascertain if the structures seen in Fig. 2(b) are resonant in nature and not due to reflections generated by the Λ^* states, it is necessary to perform a full amplitude analysis, allowing for interference effects between both decay sequences.

The fit uses five decay angles as independent variables as well as the K^-p invariant mass m_{Kp} . First we tried to fit the data with an amplitude model that contains 14 Λ^* states listed by the Particle Data Group [11]. As this did not give a satisfactory description of the data, we added one P_c^+ state, and when that was not sufficient we included a second state. The two P_c^+ states are found to have masses of $4380 \pm 8 \pm 29$ MeV and $4449.8 \pm 1.7 \pm 2.5$ MeV, with corresponding widths of $205 \pm 18 \pm 86$ MeV and $39 \pm 5 \pm 19$ MeV. (Natural units are used throughout this Letter. Whenever two uncertainties are quoted the first is statistical and the second systematic.) The fractions of the total sample due to the lower mass and higher mass states are $(8.4 \pm 0.7 \pm 4.2)\%$ and $(4.1 \pm 0.5 \pm 1.1)\%$, respectively. The best fit solution has spin-parity J^P values of $(3/2^-, 5/2^+)$. Acceptable solutions are also found for additional cases with opposite parity, either $(3/2^+, 5/2^-)$ or $(5/2^+, 3/2^-)$. The best fit projections are shown in Fig. 3. Both m_{Kp} and the peaking structure in $m_{J/\psi p}$ are reproduced. The significances of the lower mass and higher mass states are 9 and 12 standard deviations, respectively.

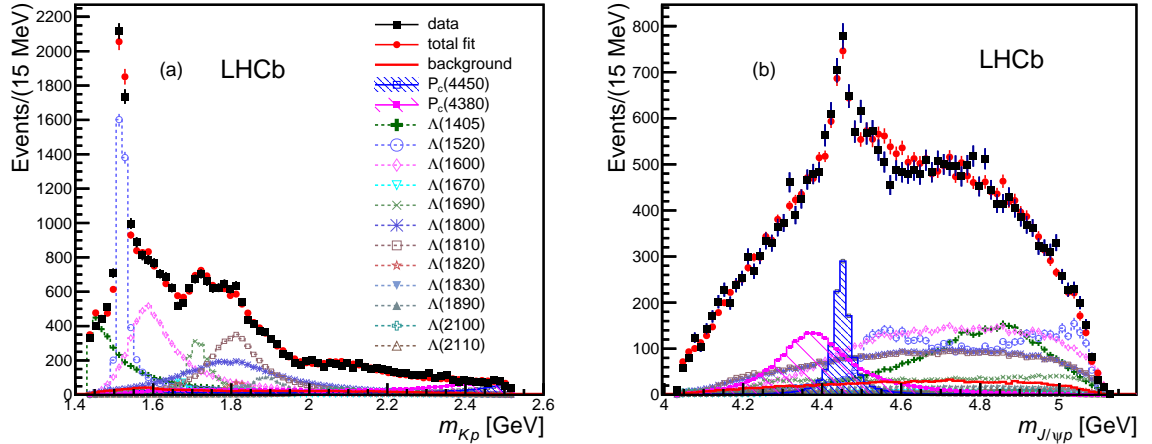


Figure 3: Fit projections for (a) m_{Kp} and (b) $m_{J/\psi p}$ for the reduced Λ^* model with two P_c^+ states (see Table 1). The data are shown as solid (black) squares, while the solid (red) points show the results of the fit. The solid (red) histogram shows the background distribution. The (blue) open squares with the shaded histogram represent the $P_c(4450)^+$ state, and the shaded histogram topped with (purple) filled squares represents the $P_c(4380)^+$ state. Each Λ^* component is also shown. The error bars on the points showing the fit results are due to simulation statistics.

Analysis and results

We use data corresponding to 1 fb^{-1} of integrated luminosity acquired by the LHCb experiment in pp collisions at 7 TeV center-of-mass energy, and 2 fb^{-1} at 8 TeV. The LHCb detector [12] is a single-arm forward spectrometer covering the pseudorapidity range $2 < \eta < 5$. The detector includes a high-precision tracking system consisting of a silicon-strip vertex detector surrounding the pp interaction region [13], a large-area silicon-strip detector located upstream of a dipole magnet with a bending power of about 4 Tm, and three stations of silicon-strip detectors and straw drift tubes [14] placed downstream of the magnet. Different types of charged hadrons are distinguished using information from two ring-imaging Cherenkov detectors [15]. Muons are identified by a system composed of alternating layers of iron and multiwire proportional chambers [16].

Events are triggered by a $J/\psi \rightarrow \mu^+\mu^-$ decay, requiring two identified muons with opposite charge, each with transverse momentum, p_T , greater than 500 MeV. The dimuon system is required to form a vertex with a fit $\chi^2 < 16$, to be significantly displaced from the nearest pp interaction vertex, and to have an invariant mass within 120 MeV of the J/ψ mass [11]. After applying these requirements, there is a large J/ψ signal over a small background [17]. Only candidates with dimuon invariant mass between -48 MeV and $+43 \text{ MeV}$ relative to the observed J/ψ mass peak are selected, the asymmetry accounting for final-state electromagnetic radiation.

Analysis preselection requirements are imposed prior to using a gradient Boosted Decision Tree, BDTG [18], that separates the A_b^0 signal from backgrounds. Each track is required to be of good quality and multiple reconstructions of the same track are removed. Requirements on the individual particles include $p_T > 550 \text{ MeV}$ for muons, and $p_T > 250 \text{ MeV}$ for hadrons. Each hadron must have an impact parameter χ^2 with respect to the primary pp interaction vertex larger than 9, and must be positively identified in the particle identification system. The K^-p system must form a vertex with $\chi^2 < 16$, as must the two muons from the J/ψ decay. Requirements on the A_b^0 candidate include a vertex $\chi^2 < 50$ for 5 degrees of freedom, and a flight distance of greater than 1.5 mm. The vector from the primary vertex to the A_b^0 vertex must align with the A_b^0 momentum so that the cosine of the angle between them is larger than 0.999. Candidate $\mu^+\mu^-$ combinations are constrained to the J/ψ mass for subsequent use in event selection.

The BDTG technique involves a “training” procedure using sideband data background and simulated signal samples. (The variables used are listed in the supplementary material.) We use 2×10^6 $A_b^0 \rightarrow J/\psi K^-p$ events with $J/\psi \rightarrow \mu^+\mu^-$ that are generated uniformly in phase space in the LHCb acceptance, using PYTHIA [19] with a special LHCb parameter tune [20], and the LHCb detector simulation based on GEANT4 [21], described in Ref. [22]. The product of the reconstruction and trigger efficiencies within the LHCb geometric acceptance is about 10%. In addition, specific backgrounds from \bar{B}_s^0 and \bar{B}^0 decays are vetoed. This is accomplished by removing combinations that when interpreted as $J/\psi K^+K^-$ fall within $\pm 30 \text{ MeV}$ of the \bar{B}_s^0 mass or when interpreted as $J/\psi K^-\pi^+$ fall within $\pm 30 \text{ MeV}$ of the \bar{B}^0 mass. This requirement effectively eliminates background from these sources and causes only smooth changes in the detection efficiencies across the

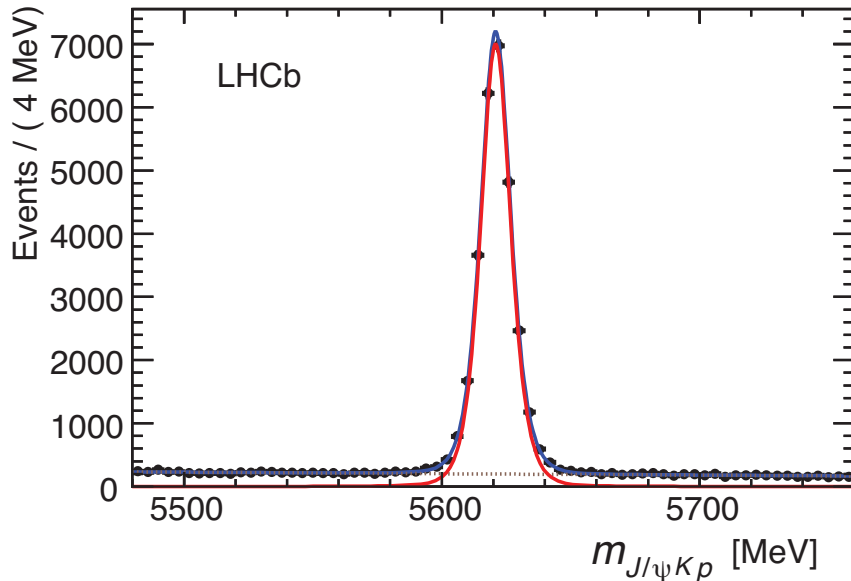


Figure 4: Invariant mass spectrum of $J/\psi K^- p$ combinations, with the total fit, signal and background components shown as solid (blue), solid (red) and dashed lines, respectively.

Λ_b^0 decay phase space. Backgrounds from Ξ_b decays cannot contribute significantly to our sample. We choose a relatively tight cut on the BDTG output variable that leaves $26\,007 \pm 166$ signal candidates containing 5.4% background within ± 15 MeV ($\pm 2\sigma$) of the $J/\psi K^- p$ mass peak, as determined by the unbinned extended likelihood fit shown in Fig. 4. The combinatorial background is modeled with an exponential function and the Λ_b^0 signal shape is parameterized by a double-sided Hypatia function [23], where the signal radiative tail parameters are fixed to values obtained from simulation. For subsequent analysis we constrain the $J/\psi K^- p$ four-vectors to give the Λ_b^0 invariant mass and the Λ_b^0 momentum vector to be aligned with the measured direction from the primary to the Λ_b^0 vertices [24].

In Fig. 5 we show the “Dalitz” plot [25] using the $K^- p$ and $J/\psi p$ invariant masses-squared as independent variables. A distinct vertical band is observed in the $K^- p$ invariant mass distribution near 2.3 GeV^2 corresponding to the $\Lambda(1520)$ resonance. There is also a distinct horizontal band near 19.5 GeV^2 . As we see structures in both $K^- p$ and $J/\psi p$ mass distributions we perform a full amplitude analysis, using the available angular variables in addition to the mass distributions, in order to determine the resonances present. No structure is seen in the $J/\psi K^-$ invariant mass.

We consider the two interfering processes shown in Fig. 1, which produce two distinct decay sequences: $\Lambda_b^0 \rightarrow J/\psi \Lambda^*$, $\Lambda^* \rightarrow K^- p$ and $\Lambda_b^0 \rightarrow P_c^+ K^-$, $P_c^+ \rightarrow J/\psi p$, with $J/\psi \rightarrow \mu^+ \mu^-$ in both cases. We use the helicity formalism [26] in which each sequential decay $A \rightarrow BC$ contributes to the amplitude a term

$$\mathcal{H}_{\lambda_B, \lambda_C}^{A \rightarrow BC} D_{\lambda_A, \lambda_B - \lambda_C}^{J_A}(\phi_B, \theta_A, 0)^* R_A(m_{BC}) = \mathcal{H}_{\lambda_B, \lambda_C}^{A \rightarrow BC} e^{i\lambda_A \phi_B} d_{\lambda_A, \lambda_B - \lambda_C}^{J_A}(\theta_A) R_A(m_{BC}), \quad (1)$$

where λ is the quantum number related to the projection of the spin of the particle onto its momentum vector (helicity) and $\mathcal{H}_{\lambda_B, \lambda_C}^{A \rightarrow BC}$ are complex helicity-coupling amplitudes

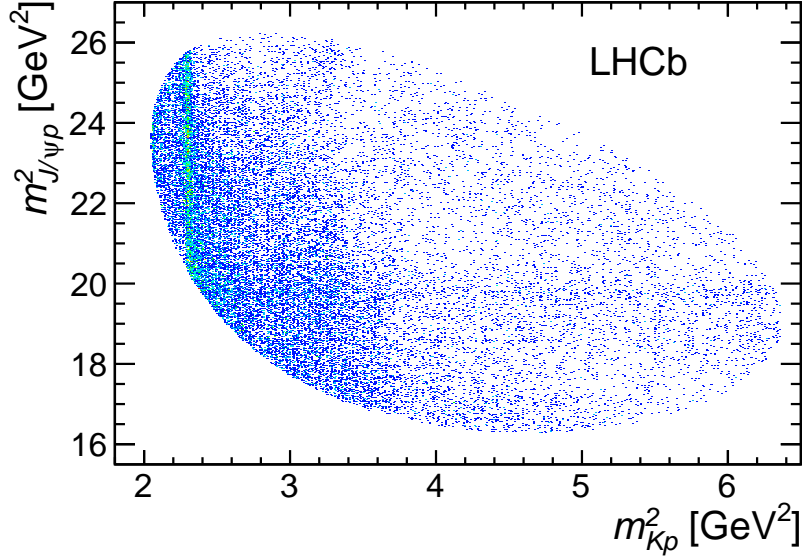


Figure 5: Invariant mass squared of K^-p versus $J/\psi p$ for candidates within ± 15 MeV of the Λ_b^0 mass.

describing the decay dynamics. Here θ_A and ϕ_B are the polar and azimuthal angles of B in the rest frame of A (θ_A is known as the “helicity angle” of A). The three arguments of Wigner’s D -matrix are Euler angles describing the rotation of the initial coordinate system with the z -axis along the helicity axis of A to the coordinate system with the z -axis along the helicity axis of B [11]. We choose the convention in which the third Euler angle is zero. In Eq. (1), $d_{\lambda_A, \lambda_B - \lambda_C}^{J_A}(\theta_A)$ is the Wigner small- d matrix. If A has a non-negligible natural width, the invariant mass distribution of the B and C daughters is described by the complex function $R_A(m_{BC})$ discussed below, otherwise $R_A(m_{BC}) = 1$.

Using Clebsch-Gordan coefficients, we express the helicity couplings in terms of LS couplings ($B_{L,S}$), where L is the orbital angular momentum in the decay, and S is the total spin of A plus B :

$$\mathcal{H}_{\lambda_B, \lambda_C}^{A \rightarrow BC} = \sum_L \sum_S \sqrt{\frac{2L+1}{2J_A+1}} B_{L,S} \begin{pmatrix} J_B & J_C & S \\ \lambda_B & -\lambda_C & \lambda_B - \lambda_C \end{pmatrix} \times \begin{pmatrix} L & S & J_A \\ 0 & \lambda_B - \lambda_C & \lambda_B - \lambda_C \end{pmatrix}, \quad (2)$$

where the expressions in parentheses are the standard Wigner 3j-symbols. For strong decays, possible L values are constrained by the conservation of parity (P): $P_A = P_B P_C (-1)^L$.

Denoting J/ψ as ψ , the matrix element for the $\Lambda_b^0 \rightarrow J/\psi \Lambda^*$ decay sequence is

$$\mathcal{M}_{\lambda_{\Lambda_b^0}, \lambda_p, \Delta\lambda_\mu}^{\Lambda^*} \equiv \sum_n \sum_{\lambda_{\Lambda^*}} \sum_{\lambda_\psi} \mathcal{H}_{\lambda_{\Lambda^*}, \lambda_\psi}^{\Lambda_b^0 \rightarrow \Lambda^* \psi} D_{\lambda_{\Lambda_b^0}, \lambda_{\Lambda^*} - \lambda_\psi}^{\frac{1}{2}}(0, \theta_{\Lambda_b^0}, 0)^* \mathcal{H}_{\lambda_p, 0}^{\Lambda^* \rightarrow Kp} D_{\lambda_{\Lambda^*}, \lambda_p}^{J_{\Lambda^*}}(\phi_K, \theta_{\Lambda^*}, 0)^* R_{\Lambda^*}(m_{Kp}) D_{\lambda_\psi, \Delta\lambda_\mu}^1(\phi_\mu, \theta_\psi, 0)^*, \quad (3)$$

where the x -axis, in the coordinates describing the Λ_b^0 decay, is chosen to fix $\phi_{\Lambda^*} = 0$. The

sum over n is due to many different Λ_n^* resonances contributing to the amplitude. Since the J/ψ decay is electromagnetic, the values of $\Delta\lambda_\mu \equiv \lambda_{\mu^+} - \lambda_{\mu^-}$ are restricted to ± 1 .

There are 4 (6) independent complex $\mathcal{H}_{\lambda_{\Lambda^*}, \lambda_\psi}^{A_b^0 \rightarrow \Lambda_n^* \psi}$ couplings to fit for each Λ_n^* resonance for $J_{\Lambda_n^*} = \frac{1}{2}$ ($> \frac{1}{2}$). They can be reduced to only 1 (3) free $B_{L,S}$ couplings to fit if only the lowest (the lowest two) values of L are considered. The mass m_{Kp} , together with all decay angles entering Eq. (3), $\theta_{A_b^0}$, θ_{Λ^*} , ϕ_K , θ_ψ and ϕ_μ (denoted collectively as Ω), constitute the six independent dimensions of the $A_b^0 \rightarrow J/\psi p K^-$ decay phase space.

Similarly, the matrix element for the P_c^+ decay chain is given by

$$\begin{aligned} \mathcal{M}_{\lambda_{A_b^0}, \lambda_p^{P_c}, \Delta\lambda_\mu^{P_c}}^{P_c} &\equiv \sum_j \sum_{\lambda_{P_c}} \sum_{\lambda_\psi^{P_c}} \mathcal{H}_{\lambda_{P_c}, 0}^{A_b^0 \rightarrow P_{c_j} K} D_{\lambda_{A_b^0}, \lambda_{P_c}}^{\frac{1}{2}}(\phi_{P_c}, \theta_{A_b^0}^{P_c}, 0)^* \\ &\quad \mathcal{H}_{\lambda_\psi^{P_c}, \lambda_p^{P_c}}^{P_{c_j} \rightarrow \psi p} D_{\lambda_{P_c}, \lambda_\psi^{P_c} - \lambda_p^{P_c}}^{J_{P_{c_j}}}(\phi_\psi, \theta_{P_c}, 0)^* R_{P_{c_j}}(m_{\psi p}) D_{\lambda_\psi^{P_c}, \Delta\lambda_\mu^{P_c}}^1(\phi_\mu^{P_c}, \theta_\psi^{P_c}, 0)^*, \end{aligned} \quad (4)$$

where the angles and helicity states carry the superscript or subscript P_c to distinguish them from those defined for the Λ^* decay chain. The sum over j allows for the possibility of contributions from more than one P_c^+ resonance. There are 2 (3) independent helicity couplings $\mathcal{H}_{\lambda_\psi^{P_c}, \lambda_p^{P_c}}^{P_{c_j} \rightarrow \psi p}$ for $J_{P_{c_j}} = \frac{1}{2}$ ($> \frac{1}{2}$), and a ratio of the two $\mathcal{H}_{\lambda_{P_c}, 0}^{A_b^0 \rightarrow P_{c_j} K}$ couplings, to determine from the data.

The mass-dependent $R_{\Lambda_n^*}(m_{Kp})$ and $R_{P_{c_j}}(m_{J/\psi p})$ terms are given by

$$R_X(m) = B'_{L_{A_b^0} X}(p, p_0, d) \left(\frac{p}{M_{A_b^0}} \right)^{L_{A_b^0}^X} \text{BW}(m|M_{0X}, \Gamma_{0X}) B'_{L_X}(q, q_0, d) \left(\frac{q}{M_{0X}} \right)^{L_X}. \quad (5)$$

Here p is the $X = \Lambda^*$ or P_c^+ momentum in the A_b^0 rest frame, and q is the momentum of either decay product of X in the X rest frame. The symbols p_0 and q_0 denote values of these quantities at the resonance peak ($m = M_{0X}$). The orbital angular momentum between the decay products of A_b^0 is denoted as $L_{A_b^0}^X$. Similarly, L_X is the orbital angular momentum between the decay products of X . The orbital angular momentum barrier factors, $p^L B'_L(p, p_0, d)$, involve the Blatt-Weisskopf functions [27], and account for the difficulty in creating larger orbital angular momentum L , which depends on the momentum of the decay products p and on the size of the decaying particle, given by the d constant. We set $d = 3.0 \text{ GeV}^{-1} \sim 0.6 \text{ fm}$. The relativistic Breit-Wigner amplitude is given by

$$\text{BW}(m|M_{0X}, \Gamma_{0X}) = \frac{1}{M_{0X}^2 - m^2 - iM_{0X}\Gamma(m)}, \quad (6)$$

where

$$\Gamma(m) = \Gamma_{0X} \left(\frac{q}{q_0} \right)^{2L_X+1} \frac{M_{0X}}{m} B'_{L_X}(q, q_0, d)^2, \quad (7)$$

is the mass dependent width of the resonance. For the $\Lambda(1405)$ resonance, which peaks below the $K^- p$ threshold, we use a two-component Flatté-like parameterization [28] (see

the supplementary material). The couplings for the allowed channels, $\Sigma\pi$ and Kp , are taken to be equal and to correspond to the nominal value of the width [11]. For all resonances we assume minimal values of $L_{A_b^0}^X$ and of L_X in $R_X(m)$. For nonresonant (NR) terms we set $\text{BW}(m) = 1$ and $M_{0\text{NR}}$ to the midrange mass.

Before the matrix elements for the two decay sequences can be added coherently, the proton and muon helicity states in the A^* decay chain must be expressed in the basis of helicities in the P_c^+ decay chain,

$$|\mathcal{M}|^2 = \sum_{\lambda_{A_b^0}} \sum_{\lambda_p} \sum_{\Delta\lambda_\mu} \left| \mathcal{M}_{\lambda_{A_b^0}, \lambda_p, \Delta\lambda_\mu}^{A^*} + e^{i\Delta\lambda_\mu\alpha_\mu} \sum_{\lambda_p^{P_c}} d_{\lambda_p^{P_c}, \lambda_p}^{\frac{1}{2}}(\theta_p) \mathcal{M}_{\lambda_{A_b^0}, \lambda_p^{P_c}, \Delta\lambda_\mu}^{P_c} \right|^2, \quad (8)$$

where θ_p is the polar angle in the p rest frame between the boost directions from the A^* and P_c^+ rest frames, and α_μ is the azimuthal angle correcting for the difference between the muon helicity states in the two decay chains. Note that $m_{\psi p}$, $\theta_{A_b^0}^{P_c}$, ϕ_{P_c} , θ_{P_c} , ϕ_ψ , $\theta_\psi^{P_c}$, $\phi_\mu^{P_c}$, θ_p and α_μ can all be derived from the values of m_{Kp} and Ω , and thus do not constitute independent dimensions in the A_b^0 decay phase space. (A detailed prescription for calculation of all the angles entering the matrix element is given in the supplementary material.)

Strong interactions, which dominate A_b^0 production at the LHC, conserve parity and cannot produce longitudinal A_b^0 polarization. Therefore, $\lambda_{A_b^0} = +1/2$ and $-1/2$ values are equally likely, which is reflected in Eq. (8). If we allow the A_b^0 polarization to vary, the data are consistent with a polarization of zero. Interferences between various A_n^* and P_{cj}^+ resonances cancel in the integrated rates unless the resonances belong to the same decay chain and have the same quantum numbers.

The matrix element given by Eq. (8) is a 6-dimensional function of m_{Kp} and Ω and depends on the fit parameters, $\vec{\omega}$, which represent independent helicity or LS couplings, and masses and widths of resonances (or Flatté parameters), $\mathcal{M} = \mathcal{M}(m_{Kp}, \Omega | \vec{\omega})$. After accounting for the selection efficiency to obtain the signal probability density function (PDF) an unbinned maximum likelihood fit is used to determine the amplitudes. Since the efficiency does not depend on $\vec{\omega}$, it is needed only in the normalization integral, which is carried out numerically by summing $|\mathcal{M}(m_{Kp}, \Omega | \vec{\omega})|^2$ over the simulated events generated uniformly in phase space and passed through the selection. (More details are given in the supplementary material.)

We use two fit algorithms, which were independently coded, and which differ in the approach used for background subtraction. In the first approach, which we refer to as cFit, the signal region is defined as $\pm 2\sigma$ around the A_b^0 mass peak. The total PDF used in the fit to the candidates in the signal region, $\mathcal{P}(m_{Kp}, \Omega | \vec{\omega})$, includes a background component with normalization fixed to be 5.4% of the total. The background PDF is found to factorize into five two-dimensional functions of m_{Kp} and of each independent angle, which are estimated using sidebands extending from 5.0σ to 13.5σ on both sides of the peak.

In the complementary approach, called sFit, no explicit background parameterization is

needed. The PDF consists of only the signal component, with the background subtracted using the sPlot technique [29] applied to the log-likelihood sum. All candidates shown in Fig. 4 are included in the sum with weights, W_i , dependent on $m_{J/\psi K p}$. The weights are set according to the signal and the background probabilities determined by the fits to the $m_{J/\psi p K}$ distributions, similar to the fit displayed in Fig. 4, but performed in 32 different bins of the two-dimensional plane of $\cos\theta_{\Lambda_b^0}$ and $\cos\theta_{J/\psi}$ to account for correlations with the mass shapes of the signal and background components. This quasi-log-likelihood sum is scaled by a constant factor, $s_W \equiv \sum_i W_i / \sum_i W_i^2$, to account for the effect of the background subtraction on the statistical uncertainty. (More details on the cFit and sFit procedures are given in the supplementary material.)

In each approach, we minimize $-2 \ln \mathcal{L}(\vec{\omega}) = -2s_W \sum_i W_i \ln \mathcal{P}(m_{K p_i}, \Omega_i | \vec{\omega})$ which gives the estimated values of the fit parameters, $\vec{\omega}_{\min}$, together with their covariance matrix ($W_i = 1$ in cFit). The difference of $-2 \ln \mathcal{L}(\vec{\omega}_{\min})$ between different amplitude models, $\Delta(-2 \ln \mathcal{L})$, allows their discrimination. For two models representing separate hypotheses, *e.g.* when discriminating between different J^P values assigned to a P_c^+ state, the assumption of a χ^2 distribution with one degree of freedom for $\Delta(-2 \ln \mathcal{L})$ under the disfavored J^P hypothesis allows the calculation of a lower limit on the significance of its rejection, *i.e.* the p-value [30]. Therefore, it is convenient to express $\Delta(-2 \ln \mathcal{L})$ values as n_σ^2 , where n_σ corresponds to the number of standard deviations in the normal distribution with the same p-value. For nested hypotheses, *e.g.* when discriminating between models without and with P_c^+ states, n_σ overestimates the p-value by a modest amount. Simulations are used to obtain better estimates of the significance of the P_c^+ states.

Since the isospin of both the Λ_b^0 and the J/ψ particles are zero, we expect that the dominant contributions in the $K^- p$ system are Λ^* states, which would be produced via a $\Delta I = 0$ process. It is also possible that Σ^* resonances contribute, but these would have $\Delta I = 1$. By analogy with kaon decays the $\Delta I = 0$ process should be dominant [31]. The list of Λ^* states considered is shown in Table 1.

Our strategy is to first try to fit the data with a model that can describe the mass and angular distributions including only Λ^* resonances, allowing all possible known states and decay amplitudes. We call this the “extended” model. It has 146 free parameters from the helicity couplings alone. The masses and widths of the Λ^* states are fixed to their PDG values, since allowing them to float prevents the fit from converging. Variations in these parameters are considered in the systematic uncertainties.

The cFit results without any P_c^+ component are shown in Fig. 6. While the $m_{K p}$ distribution is reasonably well fitted, the peaking structure in $m_{J/\psi p}$ is not reproduced. The same result is found using sFit. The speculative addition of Σ^* resonances to the states decaying to $K^- p$ does not change this conclusion.

We will demonstrate that introducing two $P_c^+ \rightarrow J/\psi p$ resonances leads to a satisfactory description of the data. When determining parameters of the P_c^+ states, we use a more restrictive model of the $K^- p$ states (hereafter referred to as the “reduced” model) that includes only the Λ^* resonances that are well motivated, and has fewer than half the number of free parameters. As the minimal $L_{\Lambda_b^0}^{A^*}$ for the spin 9/2 $\Lambda(2350)$ equals $J_{\Lambda^*} - J_{\Lambda_b^0} - J_{J/\psi} = 3$, it is extremely unlikely that this state can be produced so close to the phase space limit.

Table 1: The Λ^* resonances used in the different fits. Parameters are taken from the PDG [11]. We take $5/2^-$ for the J^P of the $\Lambda(2585)$. The number of LS couplings is also listed for both the “reduced” and “extended” models. To fix overall phase and magnitude conventions, which otherwise are arbitrary, we set $B_{0,\frac{1}{2}} = (1, 0)$ for $\Lambda(1520)$. A zero entry means the state is excluded from the fit.

State	J^P	M_0 (MeV)	Γ_0 (MeV)	# Reduced	# Extended
$\Lambda(1405)$	$1/2^-$	$1405.1^{+1.3}_{-1.0}$	50.5 ± 2.0	3	4
$\Lambda(1520)$	$3/2^-$	1519.5 ± 1.0	15.6 ± 1.0	5	6
$\Lambda(1600)$	$1/2^+$	1600	150	3	4
$\Lambda(1670)$	$1/2^-$	1670	35	3	4
$\Lambda(1690)$	$3/2^-$	1690	60	5	6
$\Lambda(1800)$	$1/2^-$	1800	300	4	4
$\Lambda(1810)$	$1/2^+$	1810	150	3	4
$\Lambda(1820)$	$5/2^+$	1820	80	1	6
$\Lambda(1830)$	$5/2^-$	1830	95	1	6
$\Lambda(1890)$	$3/2^+$	1890	100	3	6
$\Lambda(2100)$	$7/2^-$	2100	200	1	6
$\Lambda(2110)$	$5/2^+$	2110	200	1	6
$\Lambda(2350)$	$9/2^+$	2350	150	0	6
$\Lambda(2585)$?	≈ 2585	200	0	6

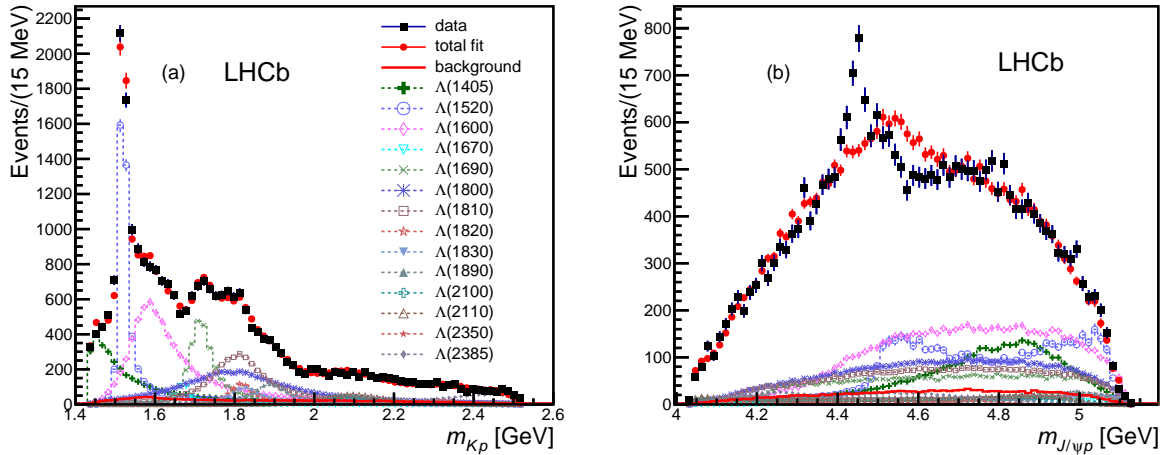


Figure 6: Results for (a) m_{Kp} and (b) $m_{J/\psi p}$ for the extended Λ^* model fit without P_c^+ states. The data are shown as (black) squares with error bars, while the (red) circles show the results of the fit. The error bars on the points showing the fit results are due to simulation statistics.

In fact $L = 3$ is the highest orbital angular momentum observed, with a very small rate, in decays of B mesons [32] with much larger phase space available ($Q = 2366$ MeV, while here $Q = 173$ MeV), and without additional suppression from the spin counting factors present in $\Lambda(2350)$ production (all three \vec{J}_{Λ^*} , $\vec{J}_{\Lambda_b^0}$ and $\vec{J}_{J/\psi}$ vectors have to line up in the same direction to produce the minimal $L_{\Lambda_b^0}^{A^*}$ value). Therefore, we eliminate it from the reduced Λ^* model. We also eliminate the $\Lambda(2585)$ state, which peaks beyond the kinematic limit and has unknown spin. The other resonances are kept but high $L_{\Lambda_b^0}^{A^*}$ amplitudes are removed; only the lowest values are kept for the high mass resonances, with a smaller reduction for the lighter ones. The number of LS amplitudes used for each resonance is listed in Table 1. With this model we reduce the number of parameters needed to describe the Λ^* decays from 146 to 64. For the different combinations of P_c^+ resonances that we try, there are up to 20 additional free parameters. Using the extended model including one resonant P_c^+ improves the fit quality, but it is still unacceptable (see supplementary material). We find acceptable fits with two P_c^+ states. We use the reduced Λ^* model for the central values of our results. The differences in fitted quantities with the extended model are included in the systematic uncertainties.

The best fit combination finds two P_c^+ states with J^P values of $3/2^-$ and $5/2^+$, for the lower and higher mass states, respectively. The $-2 \ln \mathcal{L}$ values differ by only 1 unit between the best fit and the parity reversed combination ($3/2^+$, $5/2^-$). Other combinations are less likely, although the ($5/2^+$, $3/2^-$) pair changes $-2 \ln \mathcal{L}$ by only 2.3^2 units and therefore cannot be ruled out. All combinations $1/2^\pm$ through $7/2^\pm$ were tested, and all others are disfavored by changes of more than 5^2 in the $-2 \ln \mathcal{L}$ values. The cFit results for the ($3/2^-$, $5/2^+$) fit are shown in Fig. 3. Both distributions of m_{Kp} and $m_{J/\psi p}$ are reproduced. The lower mass $3/2^-$ state has mass 4380 ± 8 MeV and width 205 ± 18 MeV, while the $5/2^+$ state has a mass of 4449.8 ± 1.7 MeV and width 39 ± 5 MeV; these errors are statistical only, systematic uncertainties are discussed later. The mass resolution is approximately 2.5 MeV and does not affect the width determinations. The sFit approach gives comparable results. The angular distributions are reasonably well reproduced, as shown in Fig. 7, and the comparison with the data in m_{Kp} intervals is also satisfactory as can be seen in Fig. 8. (A fit fraction comparison between cFit and sFit is given in the supplementary material.) The addition of further P_c^+ states does not significantly improve the fit.

Adding a single $5/2^+$ P_c^+ state to the fit with only Λ^* states reduces $-2 \ln \mathcal{L}$ by 14.7^2 using the extended model and adding a second lower mass $3/2^-$ P_c^+ state results in a further reduction of 11.6^2 . The combined reduction of $-2 \ln \mathcal{L}$ by the two states taken together is 18.7^2 . Since taking $\sqrt{\Delta 2 \ln \mathcal{L}}$ overestimates significances, we perform simulations to obtain more accurate evaluations. We generate pseudoexperiments using the null hypotheses having amplitude parameters determined by the fits to the data with no or one P_c^+ state. We fit each pseudoexperiment with the null hypothesis and with P_c^+ states added to the model. The $-2 \ln \mathcal{L}$ distributions obtained from many pseudoexperiments are consistent with χ^2 distributions with the number of degrees of freedom approximately equal to twice the number of extra parameters in the fit. Comparing these distributions with the $\Delta 2 \ln \mathcal{L}$ values from the fits to the data, p-values can be calculated. These studies show reduction

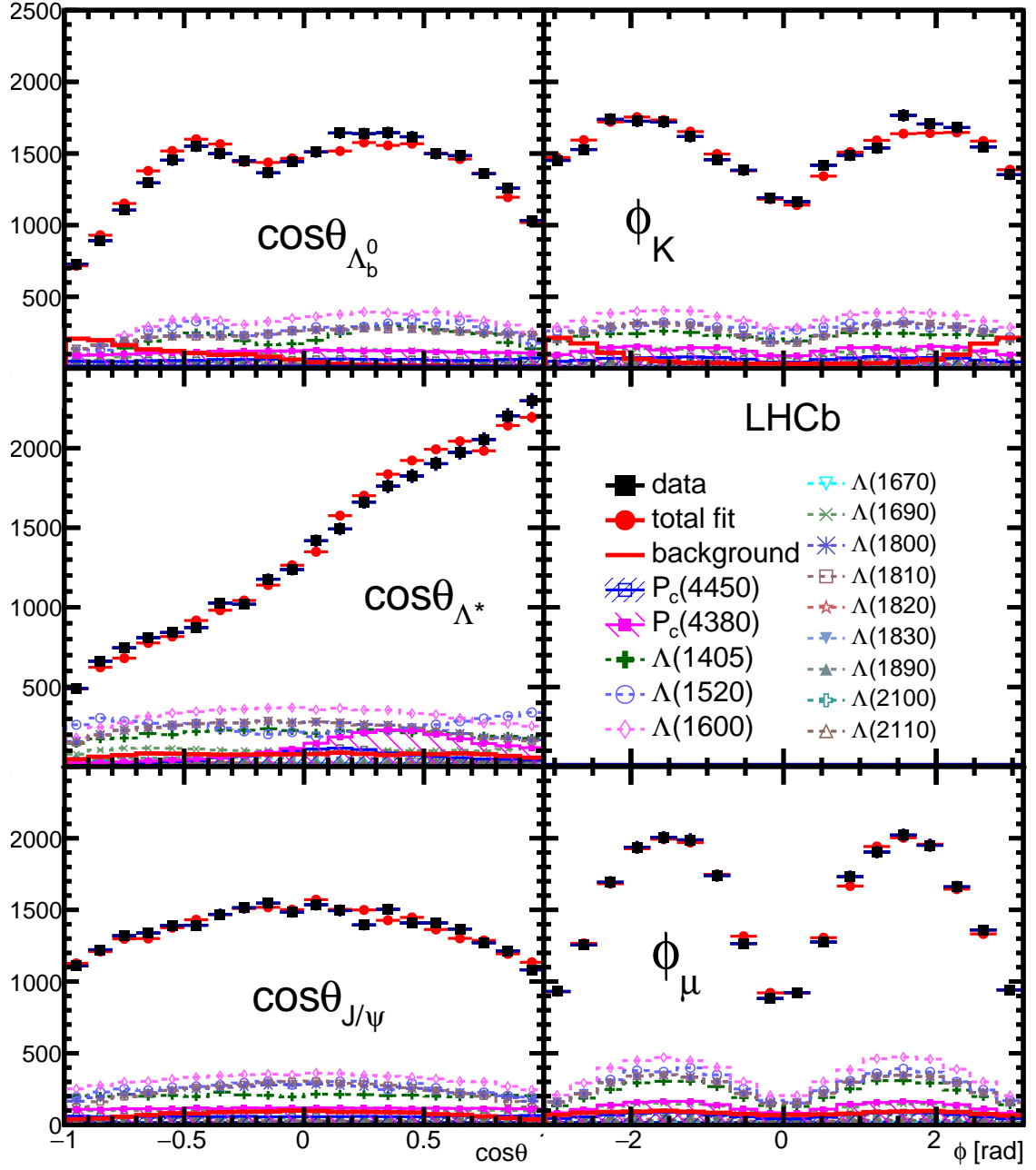


Figure 7: Various decay angular distributions for the fit with two P_c^+ states. The data are shown as (black) squares, while the (red) circles show the results of the fit. Each fit component is also shown. The angles are defined in the text.

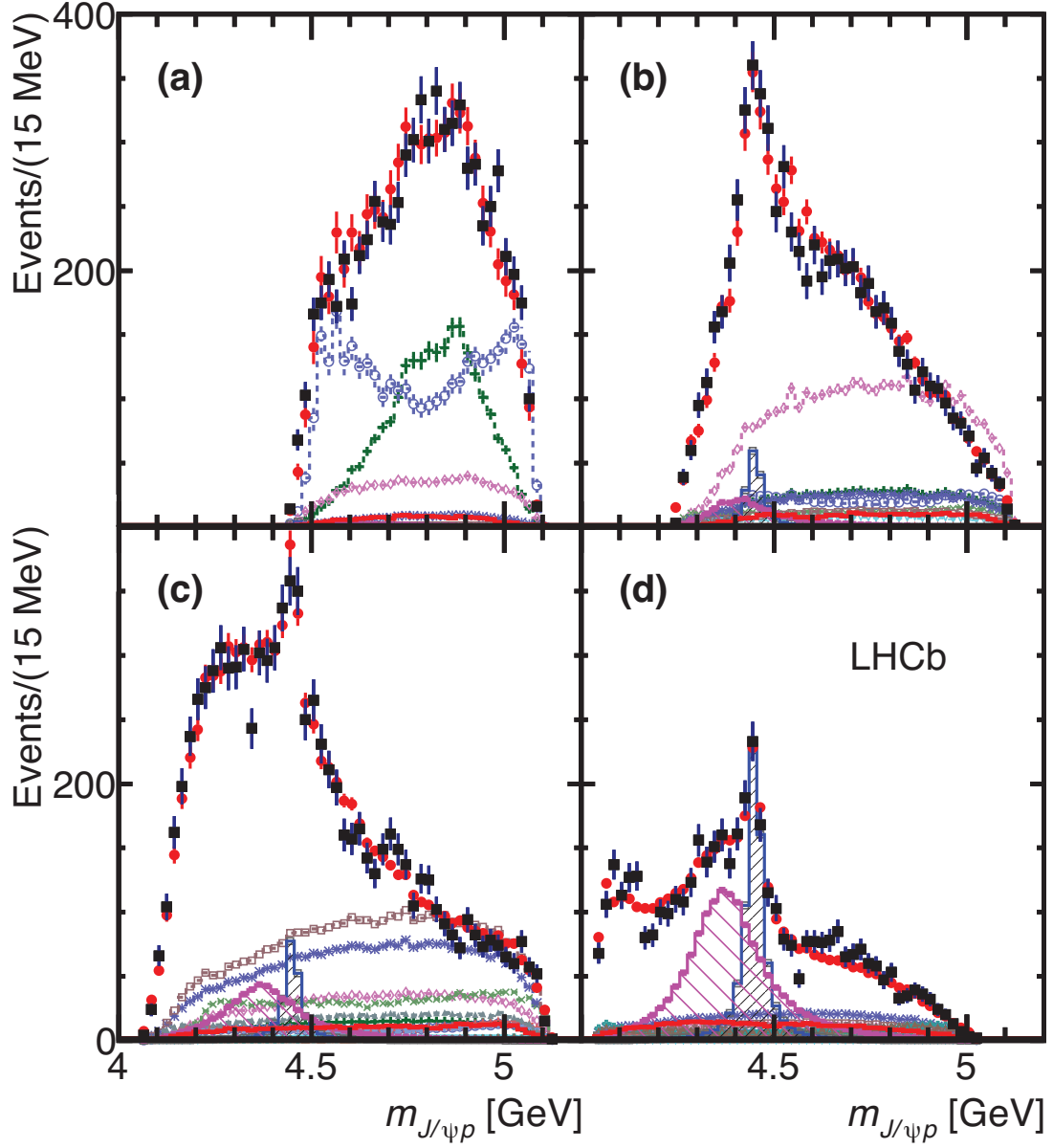


Figure 8: $m_{J/\psi p}$ in various intervals of m_{Kp} for the fit with two P_c^+ states: (a) $m_{Kp} < 1.55$ GeV, (b) $1.55 < m_{Kp} < 1.70$ GeV, (c) $1.70 < m_{Kp} < 2.00$ GeV, and (d) $m_{Kp} > 2.00$ GeV. The data are shown as (black) squares with error bars, while the (red) circles show the results of the fit. The blue and purple histograms show the two P_c^+ states. See Fig. 7 for the legend.

of the significances relative to $\sqrt{\Delta 2 \ln \mathcal{L}}$ by about 20%, giving overall significances of 9σ and 12σ , for the lower and higher mass P_c^+ states, respectively. The combined significance of two P_c^+ states is 15σ . Use of the extended model to evaluate the significance includes the effect of systematic uncertainties due to the possible presence of additional Λ^* states or higher L amplitudes.

Systematic uncertainties are evaluated for the masses, widths and fit fractions of the P_c^+ states, and for the fit fractions of the two lightest and most significant Λ^* states. Additional sources of modeling uncertainty that we have not considered may affect the fit fractions of the heavier Λ^* states. The sources of systematic uncertainties are listed in Table 2. They include differences between the results of the extended versus reduced model, varying the Λ^* masses and widths, uncertainties in the identification requirements for the proton, and restricting its momentum, inclusion of a nonresonant amplitude in the fit, use of separate higher and lower Λ_b^0 mass sidebands, alternate J^P fits, varying the Blatt-Weisskopf barrier factor, d , between 1.5 and 4.5 GeV^{-1} , changing the angular momentum L used in Eq. (5) by one or two units, and accounting for potential mismodeling of the efficiencies. For the $\Lambda(1405)$ fit fraction we also added an uncertainty for the Flatté couplings, determined by both halving and doubling their ratio, and taking the maximum deviation as the uncertainty.

Table 2: Summary of systematic uncertainties on P_c^+ masses, widths and fit fractions, and Λ^* fit fractions. A fit fraction is the ratio of the phase space integrals of the matrix element squared for a single resonance and for the total amplitude. The terms “low” and “high” correspond to the lower and higher mass P_c^+ states. The sFit/cFit difference is listed as a cross-check and not included as an uncertainty.

Source	M_0 (MeV)		Γ_0 (MeV)		Fit fractions (%)			
	low	high	low	high	low	high	$\Lambda(1405)$	$\Lambda(1520)$
Extended vs. reduced	21	0.2	54	10	3.14	0.32	1.37	0.15
Λ^* masses & widths	7	0.7	20	4	0.58	0.37	2.49	2.45
Proton ID	2	0.3	1	2	0.27	0.14	0.20	0.05
$10 < p_p < 100$ GeV	0	1.2	1	1	0.09	0.03	0.31	0.01
Nonresonant	3	0.3	34	2	2.35	0.13	3.28	0.39
Separate sidebands	0	0	5	0	0.24	0.14	0.02	0.03
J^P ($3/2^+$, $5/2^-$) or ($5/2^+$, $3/2^-$)	10	1.2	34	10	0.76	0.44		
$d = 1.5 - 4.5$ GeV^{-1}	9	0.6	19	3	0.29	0.42	0.36	1.91
$L_{\Lambda_b^0}^{P_c} \Lambda_b^0 \rightarrow P_c^+ (\text{low/high}) K^-$	6	0.7	4	8	0.37	0.16		
$L_{P_c} P_c^+ (\text{low/high}) \rightarrow J/\psi p$	4	0.4	31	7	0.63	0.37		
$L_{\Lambda_b^0}^{\Lambda^*} \Lambda_b^0 \rightarrow J/\psi \Lambda^*$	11	0.3	20	2	0.81	0.53	3.34	2.31
Efficiencies	1	0.4	4	0	0.13	0.02	0.26	0.23
Change $\Lambda(1405)$ coupling	0	0	0	0	0	0	1.90	0
Overall	29	2.5	86	19	4.21	1.05	5.82	3.89
sFit/cFit cross check	5	1.0	11	3	0.46	0.01	0.45	0.13

The stability of the results is cross-checked by comparing the data recorded in 2011/2012, with the LHCb dipole magnet polarity in up/down configurations, $\Lambda_b^0/\bar{\Lambda}_b^0$ decays, and Λ_b^0 produced with low/high values of p_T . Extended model fits without including P_c^+ states were tried with the addition of two high mass Λ^* resonances of freely varied mass and width, or four nonresonant components up to spin 3/2; these do not explain the data. The fitters were tested on simulated pseudoexperiments and no biases were found. In addition, selection requirements are varied, and the vetoes of \bar{B}_s^0 and \bar{B}^0 are removed and explicit models of those backgrounds added to the fit; all give consistent results.

Further evidence for the resonant character of the higher mass, narrower, P_c^+ state is obtained by viewing the evolution of the complex amplitude in the Argand diagram [11]. In the amplitude fits discussed above, the $P_c(4450)^+$ is represented by a Breit-Wigner amplitude, where the magnitude and phase vary with $m_{J/\psi p}$ according to an approximately circular trajectory in the $(\text{Re } A^{P_c}, \text{Im } A^{P_c})$ plane, where A^{P_c} is the $m_{J/\psi p}$ dependent part of the $P_c(4450)^+$ amplitude. We perform an additional fit to the data using the reduced Λ^* model, in which we represent the $P_c(4450)^+$ amplitude as the combination of independent complex amplitudes at six equidistant points in the range $\pm\Gamma_0 = 39 \text{ MeV}$ around $M_0 = 4449.8 \text{ MeV}$ as determined in the default fit. Real and imaginary parts of the amplitude are interpolated in mass between the fitted points. The resulting Argand diagram, shown in Fig. 9(a), is consistent with a rapid counter-clockwise change of the $P_c(4450)^+$ phase when its magnitude reaches the maximum, a behavior characteristic of a resonance. A similar study for the wider state is shown in Fig. 9(b). Although the fit does show a large phase change, the amplitude values are sensitive to the details of the Λ^* model and so this study is not conclusive.

Different binding mechanisms of pentaquark states are possible. Tight-binding was envisioned originally [2, 3]. Examples of other mechanisms include a diquark-diquark-antiquark model [33, 34], a diquark-triquark model [35], and a coupled channel model [36]. Weakly bound “molecules” of a baryon plus a meson have been also discussed [37].

Models involving thresholds or “cusps” have been invoked to explain some exotic meson candidates via nonresonant scattering mechanisms [38–40]. There are certain obvious difficulties with the use of this approach to explain our results. The closest threshold to the high mass state is at $4457.1 \pm 0.3 \text{ MeV}$ resulting from a $\Lambda_c(2595)^+ \bar{D}^0$ combination, which is somewhat higher than the peak mass value and would produce a structure with quantum numbers $J^P = 1/2^+$ which are disfavored by our data. There is no threshold close to the lower mass state.

In conclusion, we have presented a full amplitude fit to the $\Lambda_b^0 \rightarrow J/\psi K^- p$ decay. We observe significant Λ^* production recoiling against the J/ψ with the lowest mass contributions, the $\Lambda(1405)$ and $\Lambda(1520)$ states having fit fractions of $(15 \pm 1 \pm 6)\%$ and $(19 \pm 1 \pm 4)\%$, respectively. The data cannot be satisfactorily described without including two Breit-Wigner shaped resonances in the $J/\psi p$ invariant mass distribution. The significances of the lower mass and higher mass states are 9 and 12 standard deviations, respectively. These structures cannot be accounted for by reflections from $J/\psi \Lambda^*$ resonances or other known sources. Interpreted as resonant states they must have minimal quark content of $c\bar{c}uud$, and would therefore be called pentaquark-charmonium states. The lighter state

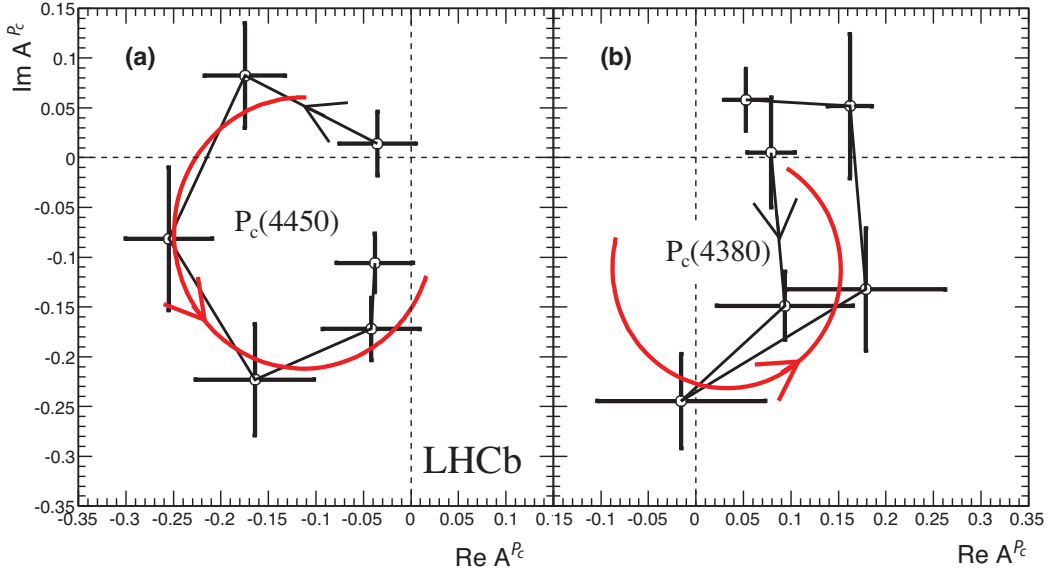


Figure 9: Fitted values of the real and imaginary parts of the amplitudes for the baseline ($3/2^-$, $5/2^+$) fit for a) the $P_c(4450)^+$ state and b) the $P_c(4380)^+$ state, each divided into six $m_{J/\psi p}$ bins of equal width between $-\Gamma_0$ and $+\Gamma_0$ shown in the Argand diagrams as connected points with error bars ($m_{J/\psi p}$ increases counterclockwise). The solid (red) curves are the predictions from the Breit-Wigner formula for the same mass ranges with M_0 (Γ_0) of 4450 (39) MeV and 4380 (205) MeV, respectively, with the phases and magnitudes at the resonance masses set to the average values between the two points around M_0 . The phase convention sets $B_{0,\frac{1}{2}} = (1, 0)$ for $A(1520)$. Systematic uncertainties are not included.

$P_c(4380)^+$ has a mass of $4380 \pm 8 \pm 29$ MeV and a width of $205 \pm 18 \pm 86$ MeV, while the heavier state $P_c(4450)^+$ has a mass of $4449.8 \pm 1.7 \pm 2.5$ MeV and a width of $39 \pm 5 \pm 19$ MeV. A model-independent representation of the $P_c(4450)^+$ contribution in the fit shows a phase change in amplitude consistent with that of a resonance. The parities of the two states are opposite with the preferred spins being $3/2$ for one state and $5/2$ for the other. The higher mass state has a fit fraction of $(4.1 \pm 0.5 \pm 1.1)\%$, and the lower mass state of $(8.4 \pm 0.7 \pm 4.2)\%$, of the total $A_b^0 \rightarrow J/\psi K^- p$ sample.

We express our gratitude to our colleagues in the CERN accelerator departments for the excellent performance of the LHC. We thank the technical and administrative staff at the LHCb institutes. We acknowledge support from CERN and from the national agencies: CAPES, CNPq, FAPERJ and FINEP (Brazil); NSFC (China); CNRS/IN2P3 (France); BMBF, DFG, HGF and MPG (Germany); INFN (Italy); FOM and NWO (The Netherlands); MNiSW and NCN (Poland); MEN/IFA (Romania); MinES and FANO (Russia); MinECo (Spain); SNSF and SER (Switzerland); NASU (Ukraine); STFC (United Kingdom); NSF (USA). The Tier1 computing centres are supported by IN2P3 (France), KIT and BMBF (Germany), INFN (Italy), NWO and SURF (The Netherlands), PIC (Spain), GridPP (United Kingdom). We are indebted to the communities behind the

multiple open source software packages on which we depend. We are also thankful for the computing resources and the access to software R&D tools provided by Yandex LLC (Russia). Individual groups or members have received support from EPLANET, Marie Skłodowska-Curie Actions and ERC (European Union), Conseil général de Haute-Savoie, Labex ENIGMASS and OCEVU, Région Auvergne (France), RFBR (Russia), XuntaGal and GENCAT (Spain), Royal Society and Royal Commission for the Exhibition of 1851 (United Kingdom).

Appendix: Supplementary material

Contents

1	Variables used in the BDTG	18
2	Additional fit results	18
2.1	Reduced model fit projections for $m_{J/\psi K^-}$	18
2.2	Extended model fit with one P_c^+ state	19
2.3	Results of extended model fit with two P_c^+ states	20
3	Fit fraction comparison between cFit and sFit	20
4	Details of the matrix element for the decay amplitude	22
4.1	Helicity formalism and notation	22
4.2	Matrix element for the Λ^* decay chain	26
4.3	Matrix element for the P_c^+ decay chain	30
4.4	Reduction of the number of helicity couplings	35
5	Details of fitting techniques	36

1 Variables used in the BDTG

Muon identification uses information from several parts of the detector, including the RICH detectors, the calorimeters and the muon system. Likelihoods are formed for the muon and pion hypotheses. The difference in the logarithms of the likelihoods, $DLL(\mu - \pi)$, is used to distinguish between the two [15]. The smaller value of the two discriminants $DLL(\mu^+ - \pi^+)$ and $DLL(\mu^- - \pi^-)$ is used as one of the BDTG variables.

The next set of variables uses the kaon and proton tracks. The χ_{IP}^2 is defined as the difference in χ^2 of the primary vertex reconstructed with and without the considered track. The smaller χ_{IP}^2 of the K^- and p is used in the BDTG. The scalar p_{T} sum of the K^- and p is another variable.

The last set of variables uses the Λ_b^0 candidate. The cosine of the angle between a vector from the primary vertex to the Λ_b^0 vertex and the Λ_b^0 momentum vector is one input variable. In addition the χ_{IP}^2 , the flight distance, the p_{T} and the vertex χ^2 of the Λ_b^0 candidate are used.

2 Additional fit results

2.1 Reduced model fit projections for $m_{J/\psi K}$

The Dalitz plots for the other two possible projections are shown in Fig. 10. There is no obvious resonance structure in the $J/\psi K^-$ mass-squared distribution.

Our fit describes well the $m_{J/\psi K}$ distribution as shown by viewing the projections of the reduced model fit. They are shown for different slices of m_{Kp} in Fig. 11.

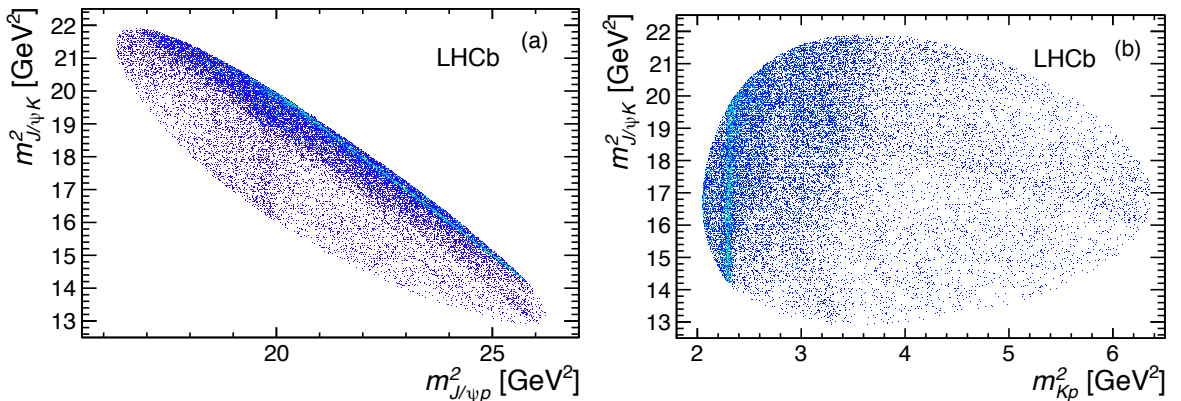


Figure 10: (a) Invariant mass squared of $J/\psi K^-$ versus $J/\psi p$ and (b) of $J/\psi K^-$ versus $K^- p$ for candidates within ± 15 MeV of the Λ_b^0 mass.

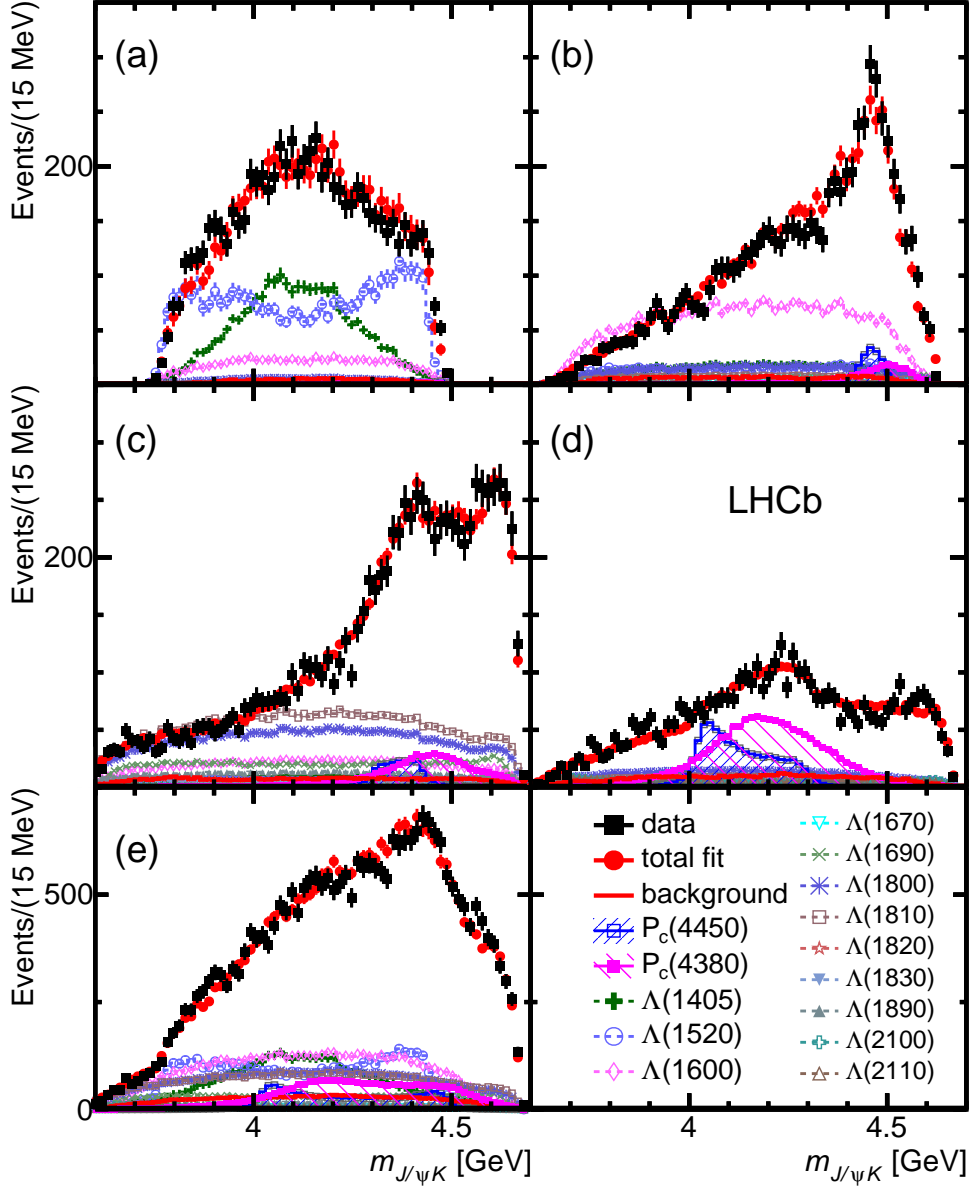


Figure 11: Projections onto $m_{J/\psi K}$ in various intervals of m_{Kp} for the reduced model fit (cFit) with two P_c^+ states of J^P equal to $3/2^-$ and $5/2^+$: (a) $m_{Kp} < 1.55$ GeV, (b) $1.55 < m_{Kp} < 1.70$ GeV, (c) $1.70 < m_{Kp} < 2.00$ GeV, (d) $m_{Kp} > 2.00$ GeV, and (e) all m_{Kp} . The data are shown as (black) squares with error bars, while the (red) circles show the results of the fit. The individual resonances are given in the legend.

2.2 Extended model fit with one P_c^+

In the fits with one P_c^+ amplitude, we test J^P values of $1/2^\pm$, $3/2^\pm$ and $5/2^\pm$. The mass and width of the putative P_c^+ state are allowed to vary. There are a total of 146 free parameters for the Λ^* states to which we add either three complex couplings for $1/2^\pm$ or

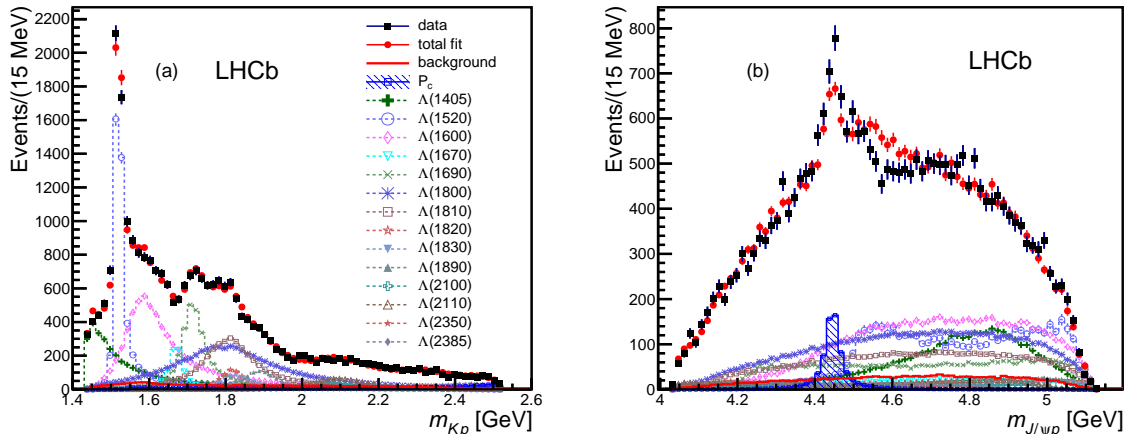


Figure 12: Results of the fit with one $J^P = 5/2^+$ P_c^+ candidate. (a) Projection of the invariant mass of K^-p combinations from $\Lambda_b^0 \rightarrow J/\psi K^-p$ candidates. The data are shown as (black) squares with error bars, while the (red) circles show the results of the fit; (b) the corresponding $J/\psi p$ mass projection. The (blue) shaded plot shows the P_c^+ projection, the other curves represent individual Λ^* states.

four for higher spins. The best fit is with a $5/2^+$ state, which improves $-2 \ln \mathcal{L}$ by 215. Figure 12 shows the projections for this fit. While the m_{Kp} projection is well described, clear discrepancies in $m_{J/\psi p}$ remain visible.

2.3 Results of extended model fit with two P_c^+ states

For completeness we include here the results of the extended model fit with two P_c^+ states using cFit. We find acceptable fits for several combinations. For a lower mass $J^P = 3/2^-$ state and a higher mass $5/2^+$ state, the masses (widths) are 4358.9 ± 6.6 MeV (151.1 ± 13.7 MeV), and 4450.1 ± 1.7 MeV (48.6 ± 4.0 MeV), respectively. The uncertainties are statistical only. The results for this two P_c^+ fit are shown in Fig. 13. Both the m_{Kp} distribution and the peaking structure in $m_{J/\psi p}$ are reproduced.

3 Fit fraction comparison between cFit and sFit

The fit fraction for a given resonance is a ratio of the phase space integrals of the matrix element squared, as given in Eq. (8), calculated for the resonance amplitude taken alone and for the total matrix element summing over all contributions. The fit fractions are listed in Table 3. The P_c^+ states have well determined fit fractions. There is good agreement between cFit and sFit. Note that the results for the $\Lambda(1405)$ resonance are based on our use of a particular Flatté amplitude model.

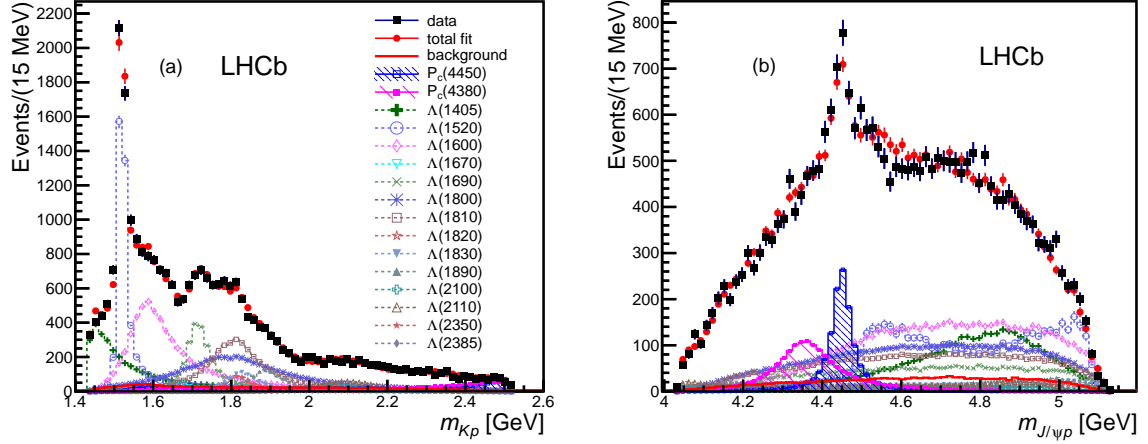


Figure 13: Results from cFit for (a) m_{Kp} and (b) $m_{J/\psi p}$ for the extended model with two P_c^+ states. The data are shown (black) squares with error bars, while the (red) circles show the results of the fit. Each Λ^* component is also shown. The (blue) open squares and (purple) solid squares show the two P_c^+ states.

Table 3: Fit fractions of the different components from cFit and sFit for the default ($3/2^-, 5/2^+$) model. Uncertainties are statistical only.

Particle	Fit fraction (%) cFit	Fit fraction (%) sFit
$P_c(4380)^+$	8.42 ± 0.68	7.96 ± 0.67
$P_c(4450)^+$	4.09 ± 0.48	4.10 ± 0.45
$\Lambda(1405)$	14.64 ± 0.72	14.19 ± 0.67
$\Lambda(1520)$	18.93 ± 0.52	19.06 ± 0.47
$\Lambda(1600)$	23.50 ± 1.48	24.42 ± 1.36
$\Lambda(1670)$	1.47 ± 0.49	1.53 ± 0.50
$\Lambda(1690)$	8.66 ± 0.90	8.60 ± 0.85
$\Lambda(1800)$	18.21 ± 2.27	16.97 ± 2.20
$\Lambda(1810)$	17.88 ± 2.11	17.29 ± 1.85
$\Lambda(1820)$	2.32 ± 0.69	2.32 ± 0.65
$\Lambda(1830)$	1.76 ± 0.58	2.00 ± 0.53
$\Lambda(1890)$	3.96 ± 0.43	3.97 ± 0.38
$\Lambda(2100)$	1.65 ± 0.29	1.94 ± 0.28
$\Lambda(2110)$	1.62 ± 0.32	1.44 ± 0.28

4 Details of the matrix element for the decay amplitude

The matrix element for $\Lambda_b^0 \rightarrow \psi K^- p$, $\psi \rightarrow \mu^+ \mu^-$ decays² must allow for various conventional $\Lambda^* \rightarrow K^- p$ resonances and exotic pentaquark states $P_c^+ \rightarrow \psi p$ that could interfere with each other.

We use the helicity formalism to write down the matrix element. To make the derivation of the matrix element easier to comprehend we start with a brief outline of this formalism and our notation. Then we discuss the application to the $\Lambda_b^0 \rightarrow \Lambda^* \psi$, $\Lambda^* \rightarrow K^- p$, $\psi \rightarrow \mu^+ \mu^-$ decay sequence, called hereafter the Λ^* decay chain matrix element. Next we discuss construction of the $\Lambda_b^0 \rightarrow P_c^+ K^-$, $P_c^+ \rightarrow \psi p$, $\psi \rightarrow \mu^+ \mu^-$ decay sequence, called hereafter the P_c decay chain matrix element, which can be coherently added to that for the Λ^* decay chain. We also discuss a possible reduction of the number of helicity couplings to be determined from the data using their relationships to the LS couplings.

4.1 Helicity formalism and notation

For each two-body decay $A \rightarrow BC$, a coordinate system is set up in the rest frame of A , with \hat{z} being³ the direction of quantization for its spin. We denote this coordinate system as $(x_0^{\{A\}}, y_0^{\{A\}}, z_0^{\{A\}})$, where the superscript “ $\{A\}$ ” means “in the rest frame of A ”, while the subscript “0” means the initial coordinates. For the first particle in the decay chain (Λ_b^0), the choice of these coordinates is arbitrary.⁴ However, once defined, these coordinates must be used consistently between all decay sequences described by the matrix element. For subsequent decays, *e.g.* $B \rightarrow DE$, the choice of these coordinates is already fixed by the transformation from the A to the B rest frames, as discussed below. Helicity is defined as the projection of the spin of the particle onto the direction of its momentum. When the z axis coincides with the particle momentum, we denote its spin projection onto it (*i.e.* the m_z quantum number) as λ . To use the helicity formalism, the initial coordinate system must be rotated to align the z axis with the direction of the momentum of one of the daughter particles, *e.g.* the B . A generalized rotation operator can be formulated in three-dimensional space, $\mathcal{R}(\alpha, \beta, \gamma)$, that uses Euler angles. Applying this operator results in a sequence of rotations: first by the angle α about the \hat{z}_0 axis, followed by the angle β about the rotated \hat{y}_1 axis and then finally by the angle γ about the rotated \hat{z}_2 axis. We use a subscript denoting the axes, to specify the rotations which have been already performed on the coordinates. The spin eigenstates of particle A , $|J_A, m_A\rangle$, in the $(x_0^{\{A\}}, y_0^{\{A\}}, z_0^{\{A\}})$ coordinate system can be expressed in the basis of its spin eigenstates, $|J_A, m'_A\rangle$, in the

²We denote J/ψ as ψ for efficiency of the notation.

³The “hat” symbol denotes a unit vector in a given direction.

⁴When designing an analysis to be sensitive (or insensitive) to a particular case of polarization, the choice is not arbitrary, but this does not change the fact that one can quantize the Λ_b^0 spin along any well-defined direction. The Λ_b^0 polarization may be different for different choices.

rotated $(x_3^{\{A\}}, y_3^{\{A\}}, z_3^{\{A\}})$ coordinate system with the help of Wigner's D -matrices

$$|J_A, m_A\rangle = \sum_{m'_A} D_{m_A, m'_A}^{J_A}(\alpha, \beta, \gamma)^* |J_A, m'_A\rangle, \quad (9)$$

where

$$D_{m, m'}^J(\alpha, \beta, \gamma)^* = \langle J, m | \mathcal{R}(\alpha, \beta, \gamma) | J, m' \rangle^* = e^{i m \alpha} d_{m, m'}^J(\beta) e^{i m' \gamma}, \quad (10)$$

and where the small- d Wigner matrix contains known functions of β that depend on J, m, m' . To achieve the rotation of the original $\hat{z}_0^{\{A\}}$ axis onto the B momentum ($\vec{p}_B^{\{A\}}$), it is sufficient to rotate by $\alpha = \phi_B^{\{A\}}$, $\beta = \theta_B^{\{A\}}$, where $\phi_B^{\{A\}}$, $\theta_B^{\{A\}}$ are the azimuthal and polar angles of the B momentum vector in the original coordinates *i.e.* $(\hat{x}_0^{\{A\}}, \hat{y}_0^{\{A\}}, \hat{z}_0^{\{A\}})$. This is depicted in Fig. 14, for the case when the quantization axis for the spin of A is its momentum in some other reference frame. Since the third rotation is not necessary, we set $\gamma = 0$.⁵ The angle $\theta_B^{\{A\}}$ is usually called “the A helicity angle”, thus to simplify the notation we will denote it as θ_A . For compact notation, we will also denote $\phi_B^{\{A\}}$ as ϕ_B . These angles can be determined from⁶

$$\begin{aligned} \phi_B &= \text{atan2} \left(p_{B\ y}^{\{A\}}, p_{B\ x}^{\{A\}} \right) \\ &= \text{atan2} \left(\hat{y}_0^{\{A\}} \cdot \vec{p}_B^{\{A\}}, \hat{x}_0^{\{A\}} \cdot \vec{p}_B^{\{A\}} \right) \\ &= \text{atan2} \left((\hat{z}_0^{\{A\}} \times \hat{x}_0^{\{A\}}) \cdot \vec{p}_B^{\{A\}}, \hat{x}_0^{\{A\}} \cdot \vec{p}_B^{\{A\}} \right), \end{aligned} \quad (11)$$

$$\cos \theta_A = \hat{z}_0^{\{A\}} \cdot \hat{p}_B^{\{A\}}. \quad (12)$$

Angular momentum conservation requires $m'_A = m'_B + m'_C = \lambda_B - \lambda_C$ (since $\vec{p}_C^{\{A\}}$ points in the opposite direction to $\hat{z}_3^{\{A\}}$, $m'_C = -\lambda_C$). Each two-body decay adds a multiplicative term to the matrix element

$$\mathcal{H}_{\lambda_B, \lambda_C}^{A \rightarrow BC} D_{m_A, \lambda_B - \lambda_C}^{J_A}(\phi_B, \theta_A, 0)^*. \quad (13)$$

The helicity couplings $\mathcal{H}_{\lambda_B, \lambda_C}^{A \rightarrow BC}$ are complex constants. Their products from subsequent decays are to be determined by the fit to the data (they represent the decay dynamics). If the decay is strong or electromagnetic, it conserves parity which reduces the number of independent helicity couplings via the relation

$$\mathcal{H}_{-\lambda_B, -\lambda_C}^{A \rightarrow BC} = P_A P_B P_C (-1)^{J_B + J_C - J_A} \mathcal{H}_{\lambda_B, \lambda_C}^{A \rightarrow BC}, \quad (14)$$

where P stands for the intrinsic parity of a particle.

⁵An alternate convention is to set $\gamma = -\alpha$. The two conventions lead to equivalent formulae.

⁶The function $\text{atan2}(x, y)$ is the $\tan^{-1}(y/x)$ function with two arguments. The purpose of using two arguments instead of one is to gather information on the signs of the inputs in order to return the appropriate quadrant of the computed angle.

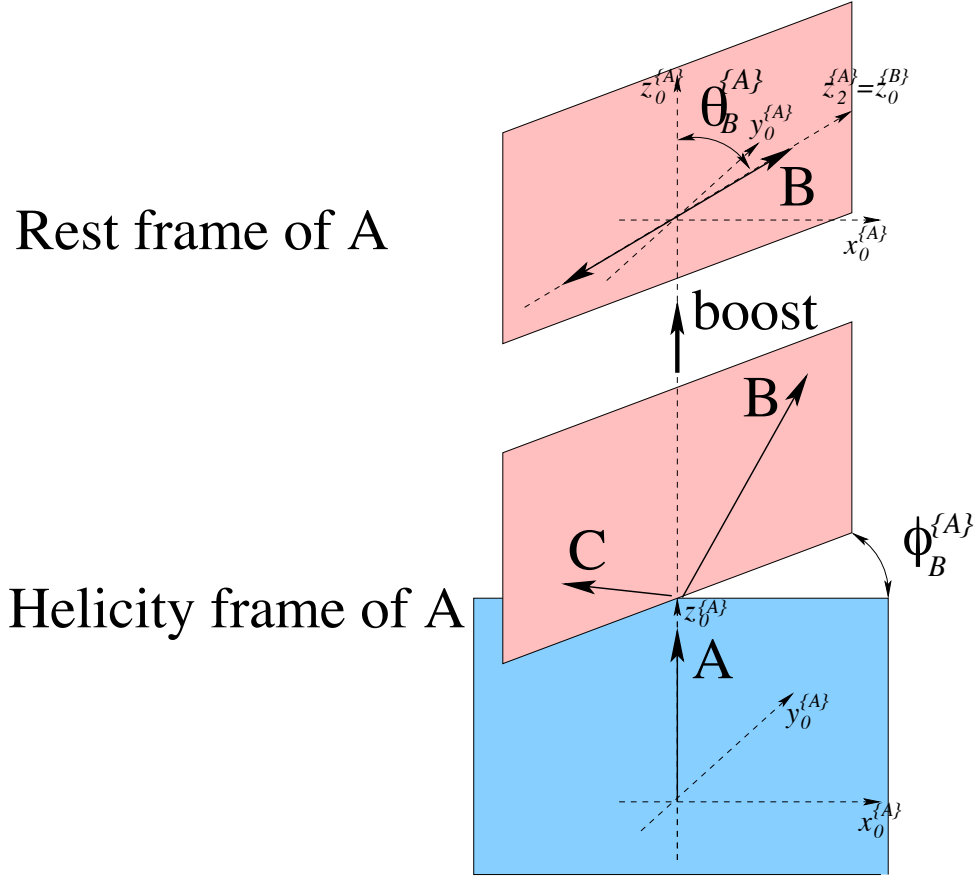


Figure 14: Coordinate axes for the spin quantization of particle A (bottom part), chosen to be the helicity frame of A ($\hat{z}_0 \parallel \vec{p}_A$ in the rest frame of its mother particle or in the laboratory frame), together with the polar ($\theta_B^{\{A\}}$) and azimuthal ($\phi_B^{\{A\}}$) angles of the momentum of its daughter B in the A rest frame (top part). Notice that the directions of these coordinate axes, denoted as $\hat{x}_0^{\{A\}}$, $\hat{y}_0^{\{A\}}$, and $\hat{z}_0^{\{A\}}$, do not change when boosting from the helicity frame of A to its rest frame. After the Euler rotation $\mathcal{R}(\alpha = \phi_B^{\{A\}}, \beta = \theta_B^{\{A\}}, \gamma = 0)$ (see the text), the rotated z axis, $\hat{z}_2^{\{A\}}$, is aligned with the B momentum; thus the rotated coordinates become the helicity frame of B . If B has a sequential decay, then the same boost-rotation process is repeated to define the helicity frame for its daughters.

After multiplying terms given by Eq. (13) for all decays in the decay sequence, they must be summed up coherently over the helicity states of intermediate particles, and incoherently over the helicity states of the initial and final-state particles. Possible helicity values of B and C particles are constrained by $|\lambda_B| \leq J_B$, $|\lambda_C| \leq J_C$ and $|\lambda_B - \lambda_C| \leq J_A$.

When dealing with the subsequent decay of the daughter, $B \rightarrow DE$, four-vectors of all particles must be first Lorentz boosted to the rest frame of B , along the $\vec{p}_B^{\{A\}}$ *i.e.* $\hat{z}_3^{\{A\}}$ direction (this is the z axis in the rest frame of A after the Euler rotations; we use the subscript “3” for the number of rotations performed on the coordinates, because of the three Euler angles, however, since we use the $\gamma = 0$ convention these coordinates are the

same as after the first two rotations). This is visualized in Fig. 14, with $B \rightarrow DE$ particle labels replaced by $A \rightarrow BC$ labels. This transformation does not change vectors that are perpendicular to the boost direction. The transformed coordinates become the initial coordinate system quantizing the spin of B in its rest frame,

$$\begin{aligned}\hat{x}_0^{\{B\}} &= \hat{x}_3^{\{A\}}, \\ \hat{y}_0^{\{B\}} &= \hat{y}_3^{\{A\}}, \\ \hat{z}_0^{\{B\}} &= \hat{z}_3^{\{A\}}.\end{aligned}\tag{15}$$

The processes of rotation and subsequent boosting can be repeated until the final-state particles are reached. In practice, there are two equivalent ways to determine the $\hat{z}_0^{\{B\}}$ direction. Using Eq. (15) we can set it to the direction of the B momentum in the A rest frame

$$\hat{z}_0^{\{B\}} = \hat{z}_3^{\{A\}} = \hat{p}_B^{\{A\}}.\tag{16}$$

Alternatively, we can make use of the fact that B and C are back-to-back in the rest frame of A , $\vec{p}_C^{\{A\}} = -\vec{p}_B^{\{A\}}$. Since the momentum of C is antiparallel to the boost direction from the A to B rest frames, the C momentum in the B rest frame will be different, but it will still be antiparallel to this boost direction

$$\hat{z}_0^{\{B\}} = -\hat{p}_C^{\{B\}}.\tag{17}$$

To determine $\hat{x}_0^{\{B\}}$ from Eq. (15), we need to find $\hat{x}_3^{\{A\}}$. After the first rotation by ϕ_B about $\hat{z}_0^{\{A\}}$, the $\hat{x}_1^{\{A\}}$ axis is along the component of $\vec{p}_B^{\{A\}}$ which is perpendicular to the $\hat{z}_0^{\{A\}}$ axis

$$\begin{aligned}\vec{a}_{B\perp z_0}^{\{A\}} &\equiv (\vec{p}_B^{\{A\}})_{\perp \hat{z}_0^{\{A\}}} = \vec{p}_B^{\{A\}} - (\vec{p}_B^{\{A\}})_{\parallel \hat{z}_0^{\{A\}}}, \\ &= \vec{p}_B^{\{A\}} - (\vec{p}_B^{\{A\}} \cdot \hat{z}_0^{\{A\}}) \hat{z}_0^{\{A\}}, \\ \hat{x}_1^{\{A\}} &= \hat{a}_{B\perp z_0}^{\{A\}} = \frac{\vec{a}_{B\perp z_0}^{\{A\}}}{|\vec{a}_{B\perp z_0}^{\{A\}}|}.\end{aligned}\tag{18}$$

After the second rotation by θ_A about $\hat{y}_1^{\{A\}}$, $\hat{z}_2^{\{A\}} \equiv \hat{z}_3^{\{A\}} = \hat{p}_B^{\{A\}}$, and $\hat{x}_2^{\{A\}} = \hat{x}_3^{\{A\}}$ is antiparallel to the component of the $\hat{z}_0^{\{A\}}$ vector that is perpendicular to the new z axis *i.e.* $\hat{p}_B^{\{A\}}$. Thus

$$\begin{aligned}\vec{a}_{z_0\perp B}^{\{A\}} &\equiv (\hat{z}_0^{\{A\}})_{\perp \hat{p}_B^{\{A\}}} = \hat{z}_0^{\{A\}} - (\hat{z}_0^{\{A\}} \cdot \hat{p}_B^{\{A\}}) \hat{p}_B^{\{A\}}, \\ \hat{x}_0^{\{B\}} &= \hat{x}_3^{\{A\}} = -\hat{a}_{z_0\perp B}^{\{A\}} = -\frac{\vec{a}_{z_0\perp B}^{\{A\}}}{|\vec{a}_{z_0\perp B}^{\{A\}}|}.\end{aligned}\tag{19}$$

Then we obtain $\hat{y}_0^{\{B\}} = \hat{z}_0^{\{B\}} \times \hat{x}_0^{\{B\}}$.

If C also decays, $C \rightarrow FG$, then the coordinates for the quantization of C spin in the C rest frame are defined by

$$\hat{z}_0^{\{C\}} = -\hat{z}_3^{\{A\}} = \hat{p}_C^{\{A\}} = -\hat{p}_B^{\{C\}}, \quad (20)$$

$$\hat{x}_0^{\{C\}} = \hat{x}_3^{\{A\}} = -\hat{a}_{z_0 \perp B}^{\{A\}} = +\hat{a}_{z_0 \perp C}^{\{A\}}, \quad (21)$$

$$\hat{y}_0^{\{C\}} = \hat{z}_0^{\{C\}} \times \hat{x}_0^{\{C\}}, \quad (22)$$

i.e. the z axis is reflected compared to the system used for the decay of particle B (it must point in the direction of C momentum in the A rest frame), but the x axis is kept the same, since we chose particle B for the rotation used in Eq. (13).

4.2 Matrix element for the Λ^* decay chain

We first discuss the part of the matrix element describing conventional $\Lambda_b^0 \rightarrow \Lambda_n^* \psi$, $\Lambda_n^* \rightarrow Kp$ decays (*i.e.* Λ^* decay chain), where Λ_n^* denotes various possible excitations of the Λ , *e.g.* $\Lambda(1520)$. For simplicity we often refer to Λ_n^* as Λ^* , unless we label an n -dependent quantity.

The weak decay $\Lambda_b^0 \rightarrow \Lambda_n^* \psi$ is described by

$$\mathcal{H}_{\lambda_{\Lambda^*}, \lambda_\psi}^{\Lambda_b^0 \rightarrow \Lambda_n^* \psi} D_{\lambda_{\Lambda_b^0}, \lambda_{\Lambda^*} - \lambda_\psi}^{\frac{1}{2}}(\phi_{\Lambda^*}, \theta_{\Lambda_b^0}, 0)^*, \quad (23)$$

where $\mathcal{H}_{\lambda_{\Lambda^*}, \lambda_\psi}^{\Lambda_b^0 \rightarrow \Lambda_n^* \psi}$ are resonance (*i.e.* n) dependent helicity couplings to be determined by a fit to the data. There are 4 different complex values of these couplings to be determined for each Λ_n^* resonance with spin $J_{\Lambda_n^*} = \frac{1}{2}$, and 6 values for higher spins. The couplings are complex parameters; thus each independent coupling contributes 2 free parameters (taken to be real and imaginary parts) to the fit. Since the ψ and Λ^* are intermediate particles in the decay chain, the matrix element terms for different values of λ_ψ and λ_{Λ^*} must be added coherently.

The choice of the $\hat{z}_0^{\{A_b^0\}}$ direction for the Λ_b^0 spin quantization is arbitrary. We choose the Λ_b^0 momentum in the lab frame to define the $\hat{z}_0^{\{A_b^0\}}$ direction, giving its spin projection onto this axis the meaning of the Λ_b^0 helicity ($\lambda_{\Lambda_b^0}$). In the Λ_b^0 rest frame, this direction is defined by the direction of the boost from the lab frame (Eq. (16)),

$$\hat{z}_0^{\{A_b^0\}} = \hat{p}_{\Lambda_b^0}^{\{\text{lab}\}}, \quad (24)$$

as depicted in Fig. 15. With this choice, $\theta_{\Lambda_b^0}$ is the Λ_b^0 helicity angle and can be calculated as

$$\cos \theta_{\Lambda_b^0} = \hat{p}_{\Lambda_b^0}^{\{\text{lab}\}} \cdot \hat{p}_{\Lambda^*}^{\{A_b^0\}}. \quad (25)$$

Longitudinal polarization of the Λ_b^0 via strong production mechanisms is forbidden due to parity conservation in strong interactions, causing $\lambda_{\Lambda_b^0} = +\frac{1}{2}$ and $-\frac{1}{2}$ to be equally likely. Terms with different $\lambda_{\Lambda_b^0}$ values must be added incoherently. The choice of $\hat{x}_0^{\{A_b^0\}}$ direction

in the Λ_b^0 rest frame is also arbitrary. We use the $\Lambda_b^0 \rightarrow \Lambda^* \psi$ decay plane in the lab frame to define it, which makes the ϕ_{Λ^*} angle zero by definition.

The strong decay $\Lambda_n^* \rightarrow K p$ is described by a term

$$\mathcal{H}_{\lambda_p}^{\Lambda_n^* \rightarrow K p} D_{\lambda_{\Lambda^*}, \lambda_p}^{J_{\Lambda_n^*}}(\phi_K, \theta_{\Lambda^*}, 0)^* R_{\Lambda_n^*}(m_{K p}). \quad (26)$$

Since the K^- meson is spinless, the resonance-dependent helicity coupling $\mathcal{H}_{\lambda_p}^{\Lambda_n^* \rightarrow K p}$ depends only on proton helicity, $\lambda_p = \pm \frac{1}{2}$. As strong decays conserve parity, the two helicity couplings are related

$$\mathcal{H}_{-\lambda_p}^{\Lambda_n^* \rightarrow K p} = -P_{\Lambda_n^*} (-1)^{J_{\Lambda_n^*} - \frac{1}{2}} \mathcal{H}_{\lambda_p}^{\Lambda_n^* \rightarrow K p}, \quad (27)$$

where $P_{\Lambda_n^*}$ is the parity of Λ_n^* . Since the overall magnitude and phase of $\mathcal{H}_{\pm \frac{1}{2}}^{\Lambda_n^* \rightarrow K p}$ can be absorbed into a redefinition of the $\mathcal{H}_{\lambda_{\Lambda^*}, \lambda_\psi}^{\Lambda_b^0 \rightarrow \Lambda_n^* \psi}$ couplings, we set $\mathcal{H}_{+\frac{1}{2}}^{\Lambda_n^* \rightarrow K p} = (1, 0)$ and $\mathcal{H}_{-\frac{1}{2}}^{\Lambda_n^* \rightarrow K p} = (P_{\Lambda_n^*} (-1)^{J_{\Lambda_n^*} - \frac{3}{2}}, 0)$, where the values in parentheses give the real and imaginary parts of the couplings.

The angles ϕ_K and θ_{Λ^*} are the azimuthal and polar angles of the kaon in the Λ^* rest frame (see Fig. 15). The $\hat{z}_0^{\{\Lambda^*\}}$ direction is defined by the boost direction from the Λ_b^0 rest frame, which coincides with the $-\vec{p}_\psi^{\{\Lambda^*\}}$ direction in this frame (Eq. (17)). This leads to

$$\cos \theta_{\Lambda^*} = -\hat{p}_\psi^{\{\Lambda^*\}} \cdot \hat{p}_K^{\{\Lambda^*\}}, \quad (28)$$

with both vectors in the Λ^* rest frame. As explained in Sec. 4.1, the $\hat{x}_0^{\{\Lambda^*\}}$ direction is defined by the choice of coordinates in the Λ_b^0 rest frame discussed above. Following

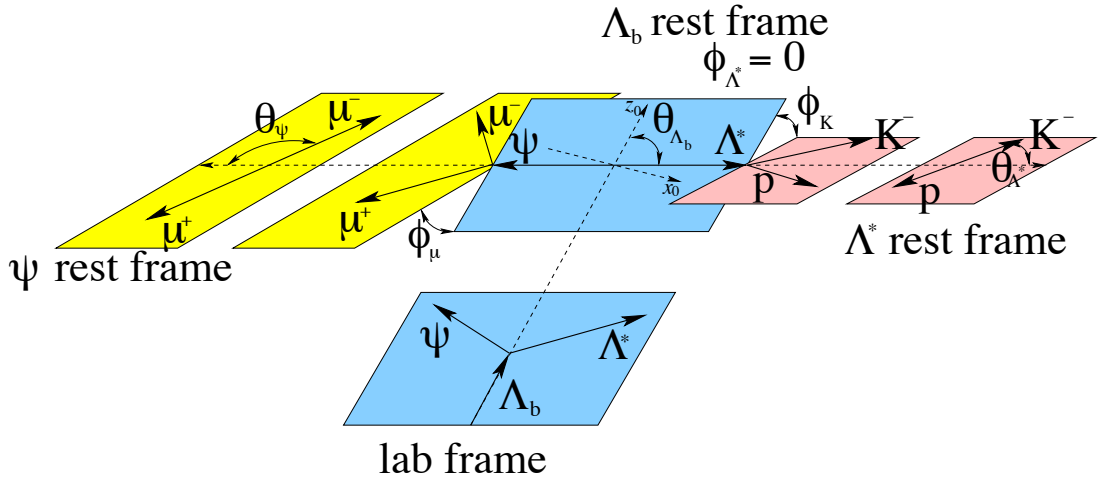


Figure 15: Definition of the decay angles in the Λ^* decay chain.

Eq. (19) and (24), we have

$$\begin{aligned}\vec{a}_{z_0 \perp \Lambda^*}^{\{A_b^0\}} &= \hat{p}_{\Lambda_b^0}^{\{\text{lab}\}} - (\hat{p}_{\Lambda_b^0}^{\{\text{lab}\}} \cdot \hat{p}_{\Lambda^*}^{\{A_b^0\}}) \hat{p}_{\Lambda^*}^{\{A_b^0\}}, \\ \hat{x}_0^{\{A^*\}} &= \hat{x}_3^{\{A_b^0\}} = -\frac{\vec{a}_{z_0 \perp \Lambda^*}^{\{A_b^0\}}}{|\vec{a}_{z_0 \perp \Lambda^*}^{\{A_b^0\}}|}.\end{aligned}\quad (29)$$

The azimuthal angle of the K^- can now be determined in the Λ^* rest frame from (Eq. (11))

$$\phi_K = \text{atan2}\left(-(\hat{p}_\psi^{\{A^*\}} \times \hat{x}_0^{\{A^*\}}) \cdot \hat{p}_K^{\{A^*\}}, \hat{x}_0^{\{A^*\}} \cdot \hat{p}_K^{\{A^*\}}\right).\quad (30)$$

The term $R_{\Lambda_n^*}(m_{Kp})$ describes the Λ_n^* resonance that appears in the invariant mass distribution of the kaon-proton system,

$$R_{\Lambda_n^*}(m_{Kp}) = B'_{L_{\Lambda_n^*}}(p, p_0, d) \left(\frac{p}{M_{\Lambda_b^0}}\right)^{L_{\Lambda_n^*}} \text{BW}(m_{Kp} | M_0^{\Lambda_n^*}, \Gamma_0^{\Lambda_n^*}) B'_{L_{\Lambda_n^*}}(q, q_0, d) \left(\frac{q}{M_0^{\Lambda_n^*}}\right)^{L_{\Lambda_n^*}}.\quad (31)$$

Here, p is the Λ^* momentum in the Λ_b^0 rest frame ($p = |\vec{p}_{\Lambda^*}^{\{A_b^0\}}|$). Similarly, q is the K^- momentum in the Λ^* rest frame ($q = |\vec{p}_K^{\{A^*\}}|$). The symbols p_0 and q_0 denote values of these quantities at the resonance peak ($m_{Kp} = M_0^{\Lambda_n^*}$). The orbital angular momentum between the Λ^* and ψ particles in the Λ_b^0 decay is denoted as $L_{\Lambda_b^0}^{\Lambda_n^*}$. Similarly, $L_{\Lambda_n^*}$ is the orbital angular momentum between the p and K^- in the Λ_n^* decay. For the orbital angular momentum barrier factors, $p^L B'_L(p, p_0, d)$, we use the Blatt-Weisskopf functions [41],

$$\begin{aligned}B'_0(p, p_0, d) &= 1, \\ B'_1(p, p_0, d) &= \sqrt{\frac{1 + (p_0 d)^2}{1 + (p d)^2}}, \\ B'_2(p, p_0, d) &= \sqrt{\frac{9 + 3(p_0 d)^2 + (p_0 d)^4}{9 + 3(p d)^2 + (p d)^4}}, \\ B'_3(p, p_0, d) &= \sqrt{\frac{225 + 45(p_0 d)^2 + 6(p_0 d)^4 + (p_0 d)^6}{225 + 45(p d)^2 + 6(p d)^4 + (p d)^6}}, \\ B'_4(p, p_0, d) &= \sqrt{\frac{11025 + 1575(p_0 d)^2 + 135(p_0 d)^4 + 10(p_0 d)^6 + (p_0 d)^8}{11025 + 1575(p d)^2 + 135(p d)^4 + 10(p d)^6 + (p d)^8}}, \\ B'_5(p, p_0, d) &= \sqrt{\frac{893025 + 99225(p_0 d)^2 + 6300(p_0 d)^4 + 315(p_0 d)^6 + 15(p_0 d)^8 + (p_0 d)^{10}}{893025 + 99225(p d)^2 + 6300(p d)^4 + 315(p d)^6 + 15(p d)^8 + (p d)^{10}}},\end{aligned}\quad (32)$$

to account for the difficulty in creating the orbital angular momentum L , which depends on the momentum of the decay products p (in the rest frame of the decaying particle) and on the size of the decaying particle given by the constant d . We set $d = 3.0 \text{ GeV}^{-1} \sim 0.6 \text{ fm}$. The relativistic Breit-Wigner amplitude is given by

$$\text{BW}(m | M_0, \Gamma_0) = \frac{1}{M_0^2 - m^2 - iM_0\Gamma(m)},\quad (33)$$

where

$$\Gamma(m) = \Gamma_0 \left(\frac{q}{q_0} \right)^{2L_{\Lambda^*} + 1} \frac{M_0}{m} B'_{L_{\Lambda^*}}(q, q_0, d)^2. \quad (34)$$

In the case of the $\Lambda(1405)$ resonance, which peaks below the K^-p threshold, we use a two-component width equivalent to the Flatté parameterization. We add to the above width in the K^-p channel, a width for its decay to the dominant $\Sigma^+\pi^-$ channel, $\Gamma(m) = \Gamma(m)_{K^-p} + \Gamma(m)_{\Sigma\pi}$, where q in the second term and q_0 in both terms are calculated assuming the decay to $\Sigma^+\pi^-$. Assuming that both channels are dynamically equally likely and differ only by the phase space factors we set Γ_0 to the total width of $\Lambda(1405)$ in both terms.

Angular momentum conservation limits $L_{\Lambda_n^*}$ to $J_{\Lambda_n^*} \pm \frac{1}{2}$, which is then uniquely defined by parity conservation in the Λ_n^* decay, $P_{\Lambda_n^*} = (-1)^{L_{\Lambda_n^*} + 1}$. Angular momentum conservation also requires $\max(J_{\Lambda_n^*} - \frac{3}{2}, 0) \leq L_{\Lambda_b^0}^* \leq J_{\Lambda_n^*} + \frac{3}{2}$. We assume the minimal value of $L_{\Lambda_b^0}^*$ in $R_{\Lambda_n^*}(m_{Kp})$.

The electromagnetic decay $\psi \rightarrow \mu^+\mu^-$ is described by a term

$$D_{\lambda_\psi, \Delta\lambda_\mu}^1(\phi_\mu, \theta_\psi, 0)^*, \quad (35)$$

where $\Delta\lambda_\mu \equiv \lambda_{\mu^+} - \lambda_{\mu^-} = \pm 1$, and ϕ_μ, θ_ψ are the azimuthal and polar angles of μ^+ for $\bar{\Lambda}_b^0$ (μ^- for Λ_b^0 decays) in the ψ rest frame (see Fig. 15). There are no helicity couplings in Eq. (35), since they are all equal due to conservation of C and P parities. Therefore, this coupling can be set to unity as its magnitude and phase can be absorbed into the other helicity couplings which are left free in the fit. The calculation of the ψ decay angles is analogous to that of the Λ^* decay angles described above (Eqs. (28)–(30))

$$\cos \theta_\psi = -\hat{p}_{\Lambda^*}^{\{\psi\}} \cdot \hat{p}_\mu^{\{\psi\}}, \quad (36)$$

$$\phi_\mu = \text{atan2} \left(-(\hat{p}_{\Lambda^*}^{\{\psi\}} \times \hat{x}_0^{\{\psi\}}) \cdot \hat{p}_\mu^{\{\psi\}}, \hat{x}_0^{\{\psi\}} \cdot \hat{p}_\mu^{\{\psi\}} \right), \quad (37)$$

with

$$\hat{x}_0^{\{\psi\}} = \hat{x}_0^{\{\Lambda^*\}} = \hat{x}_3^{\{\Lambda_b^0\}} \quad (38)$$

and $\hat{x}_3^{\{\Lambda_b^0\}}$ given by Eq. (29).

Collecting terms from the subsequent decays together, the matrix element connecting different helicity states of the initial and the final-state particles for the entire Λ^* decay chain can be written as

$$\begin{aligned} \mathcal{M}_{\lambda_{\Lambda_b^0}^{\Lambda^*}, \lambda_p, \Delta\lambda_\mu}^{\Lambda^*} &= \sum_n R_{\Lambda_n^*}(m_{Kp}) \mathcal{H}_{\lambda_p}^{\Lambda_n^* \rightarrow Kp} \sum_{\lambda_\psi} e^{i\lambda_\psi \phi_\mu} d_{\lambda_\psi, \Delta\lambda_\mu}^1(\theta_\psi) \\ &\times \sum_{\lambda_{\Lambda^*}} \mathcal{H}_{\lambda_{\Lambda^*}, \lambda_\psi}^{\Lambda_b^0 \rightarrow \Lambda_n^* \psi} e^{i\lambda_{\Lambda^*} \phi_K} d_{\lambda_{\Lambda_b^0}^0, \lambda_{\Lambda^*} - \lambda_\psi}^{\frac{1}{2}}(\theta_{\Lambda_b^0}) d_{\lambda_{\Lambda^*}, \lambda_p}^{J_{\Lambda_n^*}}(\theta_{\Lambda^*}). \end{aligned} \quad (39)$$

Terms with different helicities of the initial and final-state particles ($\lambda_p, \Delta\lambda_\mu$) must be added incoherently

$$|\mathcal{M}^{\Lambda^*}|^2 = \frac{1 + P^{A_b^0}}{2} \sum_{\lambda_p} \sum_{\Delta\lambda_\mu} \left| \mathcal{M}_{(\lambda_{A_b^0}=+1/2), \lambda_p, \Delta\lambda_\mu} \right|^2 + \frac{1 - P^{A_b^0}}{2} \sum_{\lambda_p} \sum_{\Delta\lambda_\mu} \left| \mathcal{M}_{(\lambda_{A_b^0}=-1/2), \lambda_p, \Delta\lambda_\mu} \right|^2, \quad (40)$$

where $P^{A_b^0}$ is the A_b^0 polarization, defined as the difference of probabilities for $\lambda_{A_b^0} = +1/2$ and $-1/2$ [42]. For our choice of the quantization axis for A_b^0 spin, no polarization is expected ($P^{A_b^0} = 0$) from parity conservation in strong interactions which dominate A_b^0 production at LHCb.

4.3 Matrix element for the P_c^+ decay chain

We now turn to the discussion of $A_b^0 \rightarrow P_{c_j} K^-, P_{c_j} \rightarrow \psi p$ decays, in which we allow more than one pentaquark state, $j = 1, 2, \dots$. Superscripts containing the P_c decay chain name without curly brackets, *e.g.* ϕ^{P_c} , will denote quantities belonging to this decay chain and should not be confused with the superscript “ $\{P_c\}$ ” denoting the P_c^+ rest frame, *e.g.* $\phi^{\{P_c\}}$. With only a few exceptions, we omit the Λ^* decay chain label.

The weak decay $A_b^0 \rightarrow P_{c_j} K^-$ is described by the term,

$$\mathcal{H}_{\lambda_{P_c}}^{A_b^0 \rightarrow P_{c_j} K} D_{\lambda_{A_b^0}, \lambda_{P_c}}^{\frac{1}{2}} (\phi_{P_c}, \theta_{A_b^0}^{P_c}, 0)^*, \quad (41)$$

where $\mathcal{H}_{\lambda_{P_c}}^{A_b^0 \rightarrow P_{c_j} K}$ are resonance (*i.e.* j) dependent helicity couplings. The helicity of the pentaquark state, λ_{P_c} , can take values of $\pm\frac{1}{2}$ independently of its spin, $J_{P_{c_j}} = \frac{1}{2}, \frac{3}{2}, \dots$. Therefore, there are two independent helicity couplings to be determined for each P_{c_j} state.

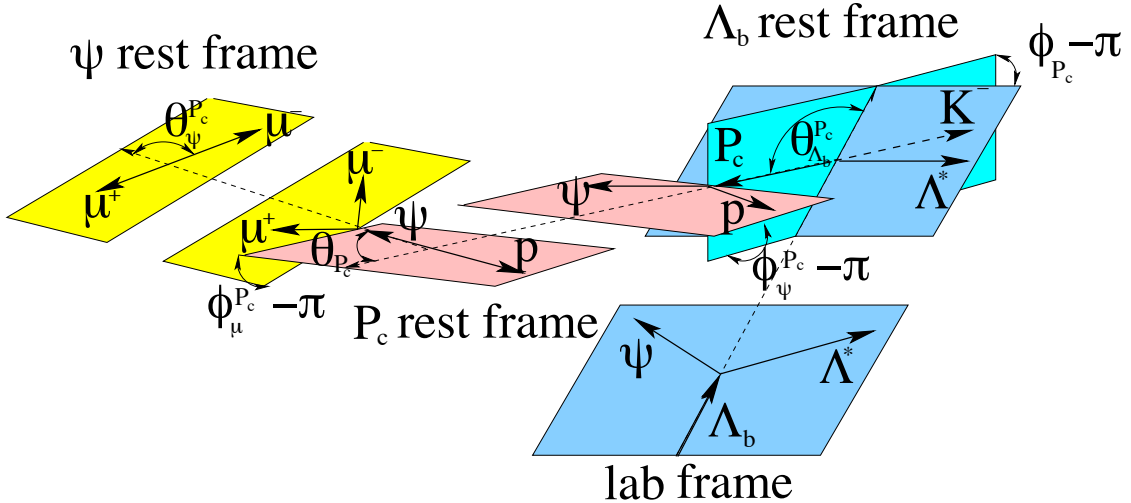


Figure 16: Definition of the decay angles in the P_c^+ decay chain.

The above mentioned ϕ_{P_c} , $\theta_{\Lambda_b^0}^{P_c}$ symbols refer to the azimuthal and polar angles of P_c in the Λ_b^0 rest frame (see Fig. 16).

Similar to Eq. (25), the Λ_b^0 helicity angle in the P_c decay chain can be calculated as,

$$\cos \theta_{\Lambda_b^0}^{P_c} = \hat{p}_{\Lambda_b^0}^{\{\text{lab}\}} \cdot \hat{p}_{P_c}^{\{\Lambda_b^0\}}. \quad (42)$$

The ϕ_{P_c} angle cannot be set to zero, since we have already defined the $\hat{x}_0^{\{\Lambda_b^0\}}$ axis in the Λ_b^0 rest frame by the $\phi_{\Lambda^*} = 0$ convention. According to Eq. (18) ($x_0^{\{\Lambda_b^0\}} = x_1^{\{\Lambda_b^0\}}$) we have:

$$\begin{aligned} \vec{a}_{\Lambda^* \perp z_0}^{\{\Lambda_b^0\}} &= \vec{p}_{\Lambda^*}^{\{\Lambda_b^0\}} - (\vec{p}_{\Lambda^*}^{\{\Lambda_b^0\}} \cdot \hat{p}_{\Lambda_b^0}^{\{\text{lab}\}}) \hat{p}_{\Lambda_b^0}^{\{\text{lab}\}}, \\ \hat{x}_0^{\{\Lambda_b^0\}} &= \frac{\vec{a}_{\Lambda^* \perp z_0}^{\{\Lambda_b^0\}}}{|\vec{a}_{\Lambda^* \perp z_0}^{\{\Lambda_b^0\}}|}. \end{aligned} \quad (43)$$

The ϕ_{P_c} angle can be determined in the Λ_b^0 rest frame from

$$\phi_{P_c} = \text{atan2} \left((\hat{p}_{\Lambda_b^0}^{\{\text{lab}\}} \times \hat{x}_0^{\{\Lambda_b^0\}}) \cdot \hat{p}_{P_c}^{\{\Lambda_b^0\}}, \hat{x}_0^{\{\Lambda_b^0\}} \cdot \hat{p}_{P_c}^{\{\Lambda_b^0\}} \right). \quad (44)$$

The strong decay $P_{c_j} \rightarrow \psi p$ is described by a term

$$\mathcal{H}_{\lambda_\psi^{P_c}, \lambda_p^{P_c}}^{P_{c_j} \rightarrow \psi p} D_{\lambda_{P_c}, \lambda_\psi^{P_c} - \lambda_p^{P_c}}^{J_{P_{c_j}}}(\phi_\psi, \theta_{P_c}, 0)^* R_{P_{c_j}}(M_{\psi p}), \quad (45)$$

where $\phi_\psi^{P_c}, \theta_{P_c}$ are the azimuthal and polar angles of the ψ in the P_c rest frame (see Fig. 16). They are defined analogously to Eqs. (28)–(30). The $\hat{z}_0^{\{P_c\}}$ direction is defined by the boost direction from the Λ_b^0 rest frame, which coincides with the $-\vec{p}_K^{\{P_c\}}$ direction. This leads to

$$\cos \theta_{P_c} = -\hat{p}_K^{\{P_c\}} \cdot \hat{p}_\psi^{\{P_c\}}. \quad (46)$$

The azimuthal angle of the ψ can now be determined in the P_c rest frame (see Fig. 16) from

$$\phi_\psi^{P_c} = \text{atan2} \left(-(\hat{p}_K^{\{P_c\}} \times \hat{x}_0^{\{P_c\}}) \cdot \hat{p}_\psi^{\{P_c\}}, \hat{x}_0^{\{P_c\}} \cdot \hat{p}_\psi^{\{P_c\}} \right). \quad (47)$$

In Eq. (45), the $\hat{x}_0^{\{P_c\}}$ direction is defined by the convention that we used in the Λ_b^0 rest frame. Thus, similar to Eq. (29) we have

$$\begin{aligned} \vec{a}_{z_0 \perp P_c}^{\{\Lambda_b^0\}} &= \hat{p}_{\Lambda_b^0}^{\{\text{lab}\}} - (\hat{p}_{\Lambda_b^0}^{\{\text{lab}\}} \cdot \hat{p}_{P_c}^{\{\Lambda_b^0\}}) \hat{p}_{P_c}^{\{\Lambda_b^0\}}, \\ \hat{x}_0^{\{P_c\}} &= -\frac{\vec{a}_{z_0 \perp P_c}^{\{\Lambda_b^0\}}}{|\vec{a}_{z_0 \perp P_c}^{\{\Lambda_b^0\}}|}. \end{aligned} \quad (48)$$

We have labeled the ψ and p helicities, $\lambda_\psi^{P_c}$ and $\lambda_p^{P_c}$, with the P_c superscript to make it clear that the spin quantization axes are different than in the Λ^* decay chain. Since the

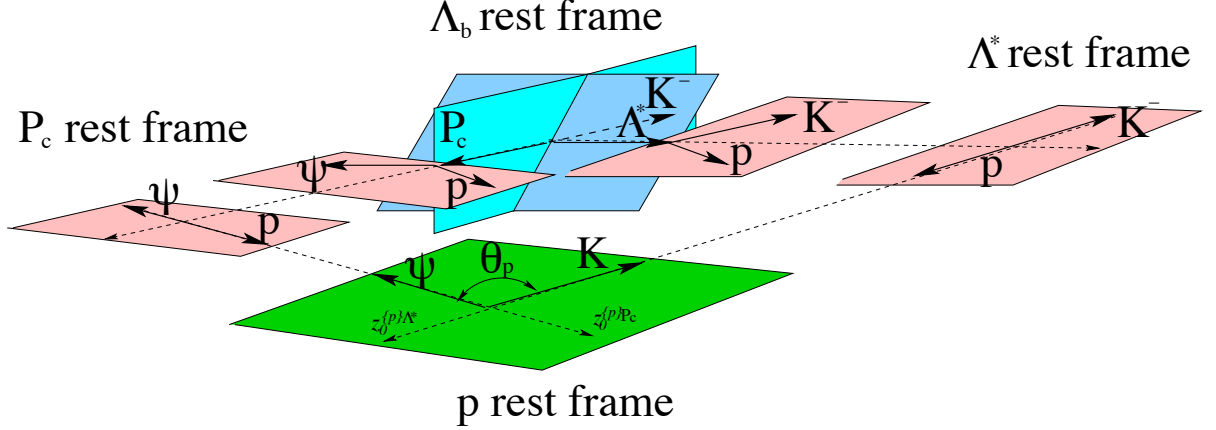


Figure 17: Definition of the θ_p angle.

ψ is an intermediate particle, this has no consequences after we sum (coherently) over $\lambda_\psi^{P_c} = -1, 0, +1$. The proton, however, is a final-state particle. Before the P_c terms in the matrix element can be added coherently to the Λ^* terms, the $\lambda_p^{P_c}$ states must be rotated to λ_p states (defined in the Λ^* decay chain). The proton helicity axes are different, since the proton comes from a decay of different particles in the two decay sequences, the Λ^* and P_c . The quantization axes are along the proton direction in the Λ^* and the P_c rest frames, thus antiparallel to the particles recoiling against the proton: the K^- and ψ , respectively. These directions are preserved when boosting to the proton rest frame (see Fig. 17). Thus, the polar angle between the two proton quantization axes (θ_p) can be determined from the opening angle between the K^- and ψ mesons in the p rest frame,

$$\cos \theta_p = \hat{p}_K^{\{p\}} \cdot \hat{p}_\psi^{\{p\}}. \quad (49)$$

(A similar problem is discussed in Ref. [43], where the two different χ_{c1} helicity frames in $B^0 \rightarrow K^+ \pi^- \chi_{c1}$ decays, in the interference of $B^0 \rightarrow K^* \chi_{c1}$, $K^* \rightarrow K^+ \pi^-$ and of $B^0 \rightarrow Z^- K^+$, $Z^- \rightarrow \chi_{c1} \pi^-$ contributions, are realigned.) The dot product above must be calculated by operating on the $\vec{p}_K^{\{p\}}$ and $\vec{p}_\psi^{\{p\}}$ vectors in the proton rest frame obtained by the same sequence of boost transformations, either according to the Λ^* or P_c decay chains, or even by a direct boost transformation from the lab frame.⁷

No azimuthal rotation is needed to align the two proton helicity frames, since the decay planes of the Λ^* and the P_c are the same (see Fig. 17). Therefore, the relation between λ_p and $\lambda_p^{P_c}$ states is

$$|\lambda_p\rangle = \sum_{\lambda_p^{P_c}} D_{\lambda_p^{P_c}, \lambda_p}^{J_p} (0, \theta_p, 0)^* |\lambda_p^{P_c}\rangle = \sum_{\lambda_p^{P_c}} d_{\lambda_p^{P_c}, \lambda_p}^{J_p} (\theta_p) |\lambda_p^{P_c}\rangle. \quad (50)$$

⁷Numerical values of momentum vector components, (p_x, p_y, p_z) , depend on the boost sequence taken and are related between different boosts via the rotation matrix. However, the dot product between the two vectors remains independent of the boost sequences.

Thus, the term given by Eq. (45) must be preceded by

$$\sum_{\lambda_p^{P_c} = \pm \frac{1}{2}} d_{\lambda_p^{P_c}, \lambda_p}^{J_p}(\theta_p). \quad (51)$$

Parity conservation in $P_{c_j} \rightarrow \psi p$ decays leads to the following relation

$$\begin{aligned} \mathcal{H}_{-\lambda_\psi^{P_c}, -\lambda_p^{P_c}}^{P_{c_j} \rightarrow \psi p} &= P_\psi P_p P_{P_{c_j}} (-1)^{J_\psi + J_p - J_{P_{c_j}}} \mathcal{H}_{\lambda_\psi^{P_c}, \lambda_p^{P_c}}^{P_{c_j} \rightarrow \psi p} \\ &= P_{P_{c_j}} (-1)^{\frac{1}{2} - J_{P_{c_j}}} \mathcal{H}_{\lambda_\psi^{P_c}, \lambda_p^{P_c}}^{P_{c_j} \rightarrow \psi p}, \end{aligned} \quad (52)$$

where $P_{P_{c_j}}$ is the parity of the P_{c_j} state. This relation reduces the number of independent helicity couplings to be determined from the data to 2 for $J_{P_{c_j}} = \frac{1}{2}$ and 3 for $J_{P_{c_j}} \geq \frac{3}{2}$. Since the helicity couplings enter the matrix element formula as a product, $\mathcal{H}_{\lambda_{P_c}}^{A_b^0 \rightarrow P_{c_j} K} \mathcal{H}_{\lambda_\psi^{P_c}, \lambda_p^{P_c}}^{P_{c_j} \rightarrow \psi p}$, the relative magnitude and phase of these two sets must be fixed by a convention. For example, $\mathcal{H}_{\lambda_{P_c} = -\frac{1}{2}}^{A_b^0 \rightarrow P_{c_j} K}$ can be set to $(1, 0)$ for every P_{c_j} resonance, in which case $\mathcal{H}_{\lambda_{P_c} = +\frac{1}{2}}^{A_b^0 \rightarrow P_{c_j} K}$ develops a meaning of the complex ratio of $\mathcal{H}_{\lambda_{P_c} = +\frac{1}{2}}^{A_b^0 \rightarrow P_{c_j} K} / \mathcal{H}_{\lambda_{P_c} = -\frac{1}{2}}^{A_b^0 \rightarrow P_{c_j} K}$, while all $\mathcal{H}_{\lambda_\psi^{P_c}, \lambda_p^{P_c}}^{P_{c_j} \rightarrow \psi p}$ couplings should have both real and imaginary parts free in the fit.

The term $R_{P_{c_j}}(M_{\psi p})$ describes the ψp invariant mass distribution of the P_{c_j} resonance and is given by Eq. (31) after appropriate substitutions. Angular momentum conservation limits $L_{A_b^0}^{P_{c_j}}$ in $A_b^0 \rightarrow P_{c_j} K^-$ decays to $J_{P_{c_j}} \pm \frac{1}{2}$. The angular momentum conservation also imposes $\max(J_{P_{c_j}} - \frac{3}{2}, 0) \leq L_{P_{c_j}} \leq J_{P_{c_j}} + \frac{3}{2}$, which is further restricted by the parity conservation in the P_{c_j} decays, $P_{P_{c_j}} = (-1)^{L_{P_{c_j}} + 1}$. We assume the minimal values of $L_{A_b^0}^{P_{c_j}}$ and of $L_{P_{c_j}}$ in $R_{P_{c_j}}(m_{\psi p})$.

The electromagnetic decay $\psi \rightarrow \mu^+ \mu^-$ in the P_c decay chain contributes a term

$$D_{\lambda_\psi^{P_c}, \Delta \lambda_\mu^{P_c}}^1(\phi_\mu^{P_c}, \theta_\psi^{P_c}, 0)^*, \quad (53)$$

which is the same as Eq. (35), except that since the ψ meson comes from the decay of different particles in the two decay chains, the azimuthal and polar angle of the muon in the ψ rest frame, $\phi_\mu^{P_c}, \theta_\psi^{P_c}$, are different from ϕ_μ, θ_ψ introduced in the Λ^* decay chain. The ψ helicity axis is along the boost direction from the P_c to the ψ rest frames, which is given by

$$\hat{z}_0^{\{\psi\} P_c} = -\hat{p}_p^{\{\psi\}}, \quad (54)$$

and so

$$\cos \theta_\psi^{P_c} = -\hat{p}_p^{\{\psi\}} \cdot \hat{p}_\mu^{\{\psi\}}. \quad (55)$$

The x axis is inherited from the P_c rest frame (Eq. (19)),

$$\begin{aligned} \vec{a}_{z_0 \perp \psi}^{\{P_c\}} &= -\vec{p}_K^{\{P_c\}} + (\vec{p}_K^{\{P_c\}} \cdot \hat{p}_\psi^{\{P_c\}}) \hat{p}_\psi^{\{P_c\}} \\ \hat{x}_0^{\{\psi\} P_c} = \hat{x}_3^{\{P_c\}} &= -\frac{\vec{a}_{z_0 \perp \psi}^{\{P_c\}}}{|\vec{a}_{z_0 \perp \psi}^{\{P_c\}}|}, \end{aligned} \quad (56)$$

which leads to

$$\phi_{\mu}^{P_c} = \text{atan2} \left(-(\hat{p}_p^{\{\psi\}} \times \hat{x}_0^{\{\psi\} P_c}) \cdot \hat{p}_{\mu}^{\{\psi\}}, \hat{x}_0^{\{\psi\} P_c} \cdot \hat{p}_{\mu}^{\{\psi\}} \right). \quad (57)$$

Since the muons are final-state particles, their helicity states in the P_c decay chain, $|\lambda_{\mu}^{P_c}\rangle$, need to be rotated to the muon helicity states in the Λ^* decay chain, $|\lambda_{\mu}\rangle$, before the P_c matrix element terms can be coherently added to the Λ^* matrix element terms. The situation is simpler than for the rotation of the proton helicities discussed above, as the muons come from the ψ decay in both decay chains. This makes the polar angle θ_{μ} (analogous to θ_p in Eq. (51)) equal to zero, which leads to $d_{\lambda_{\mu}^{P_c}, \lambda_{\mu}}^{\frac{1}{2}}(0) = \delta_{\lambda_{\mu}^{P_c}, \lambda_{\mu}}$, where $\delta_{i,j}$ is the Kronecker symbol. However, the muon helicity states are not identical since the x axes are offset by the azimuthal angle α_{μ} . Since the boost to the μ rest frame is the same for both decay chains (*i.e.* always from the ψ rest frame), we can determine α_{μ} in the ψ rest frame

$$\alpha_{\mu} = \text{atan2} \left((\hat{z}_3^{\{\psi\}} \times \hat{x}_3^{\{\psi\} P_c}) \cdot \hat{x}_3^{\{\psi\} \Lambda^*}, \hat{x}_3^{\{\psi\} P_c} \cdot \hat{x}_3^{\{\psi\} \Lambda^*} \right), \quad (58)$$

where $\hat{z}_3^{\{\psi\}} = \hat{p}_{\mu}^{\{\psi\}}$, and from Eq. (19)

$$\hat{x}_3^{\{\psi\} P_c} = -\hat{a}_{z_0 \perp \mu}^{\{\psi\} P_c}, \quad (59)$$

$$\vec{a}_{z_0 \perp \mu}^{\{\psi\} P_c} = -\hat{p}_p^{\{\psi\}} + (\hat{p}_p^{\{\psi\}} \cdot \hat{p}_{\mu}^{\{\psi\}}) \hat{p}_{\mu}^{\{\psi\}}, \quad (60)$$

as well as

$$\hat{x}_3^{\{\psi\} \Lambda^*} = -\hat{a}_{z_0 \perp \mu}^{\{\psi\} \Lambda^*}, \quad (61)$$

$$\vec{a}_{z_0 \perp \mu}^{\{\psi\} \Lambda^*} = -\hat{p}_{\Lambda^*}^{\{\psi\}} + (\hat{p}_{\Lambda^*}^{\{\psi\}} \cdot \hat{p}_{\mu}^{\{\psi\}}) \hat{p}_{\mu}^{\{\psi\}}. \quad (62)$$

The term aligning the muon helicity states between the two reference frames is given by

$$\sum_{\lambda_{\mu}^{P_c}} D_{\lambda_{\mu}^{P_c} \lambda_{\mu}}^{J_{\mu}^{P_c}} (\alpha_{\mu}, 0, 0)^* = \sum_{\lambda_{\mu}^{P_c}} e^{i \lambda_{\mu}^{P_c} \alpha_{\mu}} \delta_{\lambda_{\mu}^{P_c}, \lambda_{\mu}} = e^{i \lambda_{\mu} \alpha_{\mu}}. \quad (63)$$

The transformation of μ^- states will be similar to that of the μ^+ states, except that since \hat{z}_{ψ} will have the opposite direction, $\alpha_{\mu^+} = -\alpha_{\mu^-}$. The transformation of $|\lambda_{\mu^+}^{P_c}\rangle |\lambda_{\mu^-}^{P_c}\rangle$ to $|\lambda_{\mu^+}\rangle |\lambda_{\mu^-}\rangle$ states will require multiplying the terms for the P_c decay chain by

$$e^{i \lambda_{\mu} \alpha_{\mu}} e^{i \lambda_{\bar{\mu}} \alpha_{\bar{\mu}}} = e^{i (\lambda_{\mu} - \lambda_{\bar{\mu}}) \alpha_{\mu}} = e^{i \Delta \lambda_{\mu} \alpha_{\mu}}. \quad (64)$$

An alternative derivation of Eq. (64) is discussed in Ref. [7] (Eqs. (20)–(22) therein) for the interference of $B^0 \rightarrow K^* \psi$, $K^* \rightarrow K \pi$ and of $B^0 \rightarrow Z K^-$, $Z \rightarrow \psi \pi$ ($\psi \rightarrow \ell^+ \ell^-$) terms, which are analogous to the two decay chains discussed here with the substitution $B^0 \rightarrow \Lambda_b^0$, $K^* \rightarrow \Lambda^*$, $Z \rightarrow P_c$ and $\pi \rightarrow p$. The rotation by α_{μ} about the ℓ^+ direction in the ψ rest frame in the Z decay chain is incorporated by setting $\gamma = \alpha_{\mu}$, instead of $\gamma = 0$ in Eq. (53). This leads to the same formulae since

$$D_{\lambda_{\psi}^{P_c}, \Delta \lambda_{\mu}}^1 (\phi_{\mu}^{P_c}, \theta_{\psi}^{P_c}, \alpha_{\mu})^* = D_{\lambda_{\psi}^{P_c}, \Delta \lambda_{\mu}}^1 (\phi_{\mu}^{P_c}, \theta_{\psi}^{P_c}, 0)^* e^{i \Delta \lambda_{\mu} \alpha_{\mu}}. \quad (65)$$

We use the more generic derivation here to demonstrate that the methods of transforming the muon and proton helicity states between the two decay chains are the same.

Collecting terms from the three subsequent decays in the P_c chain together,

$$\begin{aligned} \mathcal{M}_{\lambda_{A_b^0}, \lambda_p^{P_c}, \Delta\lambda_\mu^{P_c}}^{P_c} &= e^{i\lambda_{A_b^0}\phi_{P_c}} \sum_j R_{P_{c_j}}(M_{\psi p}) \sum_{\lambda_\psi^{P_c}} e^{i\lambda_\psi^{P_c}\phi_\mu^{P_c}} d_{\lambda_\psi^{P_c}, \Delta\lambda_\mu}^1(\theta_\psi^{P_c}) \\ &\times \sum_{\lambda_{P_c}} \mathcal{H}_{\lambda_{P_c}}^{A_b^0 \rightarrow P_{c_j} K} e^{i\lambda_{P_c}\phi_\psi^{P_c}} d_{\lambda_{A_b^0}, \lambda_{P_c}}^{\frac{1}{2}}(\theta_{A_b^0}^{P_c}) \mathcal{H}_{\lambda_\psi^{P_c}, \lambda_p^{P_c}}^{P_{c_j} \rightarrow \psi p} d_{\lambda_{P_c}, \lambda_\psi^{P_c} - \lambda_p^{P_c}}^{J_{P_{c_j}}}(\theta_{P_c}), \end{aligned} \quad (66)$$

and adding them coherently to the Λ^* matrix element, via appropriate relation of $|\lambda_p\rangle|\lambda_{\mu^+}\rangle|\lambda_{\mu^-}\rangle$ to $|\lambda_p^{P_c}\rangle|\lambda_{\mu^+}^{P_c}\rangle|\lambda_{\mu^-}^{P_c}\rangle$ states as discussed above, leads to the final matrix element squared

$$|\mathcal{M}|^2 = \sum_{\lambda_{A_b^0} = \pm\frac{1}{2}} \sum_{\lambda_p = \pm\frac{1}{2}} \sum_{\Delta\lambda_\mu = \pm 1} \left| \mathcal{M}_{\lambda_{A_b^0}, \lambda_p, \Delta\lambda_\mu}^{\Lambda^*} + e^{i\Delta\lambda_\mu\alpha_\mu} \sum_{\lambda_p^{P_c}} d_{\lambda_p^{P_c}, \lambda_p}^{\frac{1}{2}}(\theta_p) \mathcal{M}_{\lambda_{A_b^0}, \lambda_p^{P_c}, \Delta\lambda_\mu}^{P_c} \right|^2, \quad (67)$$

where we set $P_{A_b^0} = 0$. As a cross-check, fitting the Λ_b^0 polarization to the data with the default Λ^* and P_c^+ model yields a value consistent with zero, $P_{A_b^0} = (-2.0 \pm 2.3)\%$ (statistical error only).

Assuming approximate CP symmetry, the helicity couplings for Λ_b^0 and $\bar{\Lambda}_b^0$ can be made equal, but the calculation of the angles requires some care, since parity (P) conservation does not change polar (i.e. helicity) angles, but does change azimuthal angles. Thus, not only must \vec{p}_{μ^+} be used instead of \vec{p}_{μ^-} for $\bar{\Lambda}_b^0$ candidates (with K^+ and \bar{p} in the final-state) in Eqs. (36), (37), (55), (57) and (58), but also all azimuthal angles must be reflected before entering the matrix element formula: $\phi_K \rightarrow -\phi_K$, $\phi_\mu \rightarrow -\phi_\mu$, $\phi_{P_c} \rightarrow -\phi_{P_c}$, $\phi_\psi^{P_c} \rightarrow -\phi_\psi^{P_c}$, $\phi_\mu^{P_c} \rightarrow -\phi_\mu^{P_c}$ and $\alpha_\mu \rightarrow -\alpha_\mu$ [7].

It is clear from Eq. (67) that various Λ_n^* and P_c resonances interfere in the differential distributions. By integrating the matrix element squared over the entire phase space the interferences cancel in the integrated rates unless the resonances belong to the same decay chain and have the same quantum numbers.⁸

4.4 Reduction of the number of helicity couplings

A possible reduction of the helicity couplings can be achieved by relating them to the LS couplings ($B_{L,S}$) using Clebsch-Gordan coefficients

$$\mathcal{H}_{\lambda_B, \lambda_C}^{A \rightarrow BC} = \sum_L \sum_S \sqrt{\frac{2L+1}{2J_A+1}} B_{L,S} \left(\begin{array}{cc|c} J_B & J_C & S \\ \lambda_B & -\lambda_C & \lambda_B - \lambda_C \end{array} \right) \times \left(\begin{array}{cc|c} L & S & J_A \\ 0 & \lambda_B - \lambda_C & \lambda_B - \lambda_C \end{array} \right), \quad (68)$$

⁸For $\Lambda_n^* - P_c$, the $\lambda_{A_b^0} = +1/2$ interference terms have the opposite effect to the $\lambda_{A_b^0} = -1/2$ interference terms.

and then restricting the L values. Here L is the orbital angular momentum in the decay, and S is the total spin of the daughters, $\vec{S} = \vec{J}_B + \vec{J}_C$ ($|J_B - J_C| \leq S \leq J_B + J_C$). If the energy release in the decay, $Q = M_A - M_B - M_C$, is small, $Q/M_A \ll 1$, then higher values of L should be suppressed; this effect is usually called “the angular momentum barrier.” Applying this approach to $\Lambda_b^0 \rightarrow \psi \Lambda_n^*$ decays, the lowest $L_{\Lambda_b^0}^{A_n^*}$ value (L_{\min}) corresponds to a single possible value of S , thus reducing the number of couplings to fit, from 4 ($J_{\Lambda_n^*} = \frac{1}{2}$) or 6 ($J_{\Lambda_n^*} \geq \frac{3}{2}$), to just one $B_{L,S}$ coupling per resonance. Accepting also $L_{\min} + 1$ values, gives three $B_{L,S}$ couplings to fit per resonance.

In $\Lambda_b^0 \rightarrow P_{c_j} K^-$ decays, $S = J_{P_{c_j}}$ and $L_{\Lambda_b^0}^{P_{c_j}} = J_{P_{c_j}} \pm \frac{1}{2}$. Taking only the lower $L_{\Lambda_b^0}^{P_{c_j}}$ value reduces the number of couplings from 2 to 1. Since its magnitude and phase convention can be absorbed into $\mathcal{H}_{\lambda_{\psi}^{P_{c_j}}, \lambda_{P_c}^{P_{c_j}}}^{P_{c_j} \rightarrow \psi p}$ (see the discussion in Sec. 4.3), one can simply set $B_{J_{P_{c_j}} - \frac{1}{2}, J_{P_{c_j}}}^{\Lambda_b^0 \rightarrow P_{c_j} K} = (1, 0)$ in this approach.

The reduction of couplings to fit for $P_{c_j} \rightarrow \psi p$ decays depends on the spin and parity of the P_{c_j} state. S can take values of $\frac{1}{2}$ and $\frac{3}{2}$. Values of $L_{P_{c_j}}$ must be odd (even) for even (odd) $J_{P_{c_j}}$. For a $J_{P_{c_j}}^P = \frac{1}{2}^+$ state, only $L_{P_{c_j}} = 1$ is allowed with the two possible values of S . Therefore, no reduction of couplings is possible. For a $J_{P_{c_j}}^P = \frac{1}{2}^-$ state, $L_{P_{c_j}} = 0, 2$ are allowed, each corresponding to one S value. Therefore, the number of couplings to fit can be reduced from 2 to 1 when taking $L_{P_{c_j}} = 0$. Gains can be larger for $J_{P_{c_j}} \geq \frac{3}{2}$ states.

Even if no reduction in parameters is achieved, expressing the helicity couplings via corresponding $B_{L,S}$ couplings using Eq. (68) is useful, since it automatically implements the parity constraints (Eq. (52)) by restricting possible L values. Since the overall magnitude of the matrix element does not affect the normalized signal PDF, and because its overall phase also drops out when taking its modulus, we fix the magnitude and phase convention by setting $B_{0, \frac{1}{2}}^{\Lambda_b^0 \rightarrow \Lambda(1520) J/\psi} = (1, 0)$.

5 Details of fitting techniques

The matrix element given by Eq. (67), is a 6-dimensional (6D) function of m_{Kp} and Ω and depends on the fit parameters, $\vec{\omega}$, which represent independent helicity or LS couplings, and possibly masses and widths of resonances, $\mathcal{M}(m_{Kp}, \Omega | \vec{\omega})$. We perform an unbinned maximum likelihood fit of these parameters to the 6D data by minimizing $-2 \ln \mathcal{L}(\vec{\omega}) = -2 \ln \sum_i \mathcal{P}(m_{Kp}, \Omega_i | \vec{\omega})$ with respect to $\vec{\omega}$. The signal PDF is obtained by multiplying the matrix element squared with the selection efficiency, $\epsilon(m_{Kp}, \Omega)$,

$$\mathcal{P}_{\text{sig}}(m_{Kp}, \Omega | \vec{\omega}) = \frac{1}{I(\vec{\omega})} |\mathcal{M}(m_{Kp}, \Omega | \vec{\omega})|^2 \Phi(m_{Kp}) \epsilon(m_{Kp}, \Omega), \quad (69)$$

where $\Phi(m_{Kp})$ is the phase space function equal to $p q$, where p is the momentum of the Kp system (*i.e.* Λ^*) in the Λ_b^0 rest frame, and q is the momentum of K^- in the Λ^* rest frame, and $I(\vec{\omega})$ is the normalization integral.

We use two fit algorithms that were independently coded and that differ in the approach used for background subtraction. The sFit procedure uses the sPlot technique described in Ref. [29] to subtract background from the log-likelihood sum. It has been used in previous LHCb analyses, *e.g.* measurement of ϕ_s in $B_s^0 \rightarrow J/\psi \phi$ decays [44]. The data in the entire 5480 – 5760 MeV range are passed to the fitter. Candidates are assigned “sWeights” (W_i) according to their $m_{J/\psi pK}$ value with the signal and background probabilities determined by the fit to the $m_{J/\psi pK}$ distribution,

$$-2 \ln \mathcal{L}(\vec{\omega}) = -2s_W \sum_i W_i \ln \mathcal{P}(m_{Kp i}, \Omega_i | \vec{\omega}), \quad (70)$$

where $s_W \equiv \sum_i W_i / \sum_i W_i^2$ is a constant factor accounting for the effect of the background subtraction on the statistical uncertainty. Candidates in the sideband region have negative sWeights which on average compensate for the background events present in the peak region, where events have positive sWeights. From signal simulations, we see significant variations of $\Lambda_b^0 \rightarrow J/\psi pK^-$ invariant mass resolution as functions of $\cos \theta_{\Lambda_b^0}$ and $\cos \theta_{J/\psi}$. The background distributions also vary in intensity and shape with these two variables. No strong variation is seen for the other fitting observables. To determine the sWeights, the events are divided into $4 |\cos \theta_{J/\psi}| \times 8 \cos \theta_{\Lambda_b^0}$ bins. A separate fit to the $\Lambda_b^0 \rightarrow J/\psi pK^-$ invariant mass distribution of each bin is performed.

In the sFit approach the total PDF is equal to the signal PDF, as the background is subtracted from the log-likelihood sum using sWeights,

$$\begin{aligned} -2 \ln \mathcal{L}(\vec{\omega}) &= -2s_W \sum_i W_i \ln \mathcal{P}_{\text{sig}}(m_{Kp i}, \Omega_i | \vec{\omega}) \\ &= -2s_W \sum_i W_i \ln |\mathcal{M}(m_{Kp i}, \Omega_i | \vec{\omega})|^2 + 2s_W \ln I(\vec{\omega}) \sum_i W_i \\ &\quad - 2s_W \sum_i W_i \ln [\Phi(m_{Kp i}) \epsilon(m_{Kp i}, \Omega_i)]. \end{aligned} \quad (71)$$

The last term does not depend on the fitted parameters $\vec{\omega}$ and is therefore dropped. The efficiency still appears in the normalization integral. The integration is done without the need to parameterize the efficiency, by summing the matrix element squared over the simulated events that are generated uniformly in phase space and passed through the detector modeling and the data selection procedure,

$$\begin{aligned} I(\vec{\omega}) &\equiv \int |\mathcal{M}(m_{Kp}, \Omega | \vec{\omega})|^2 \Phi(m_{Kp}) \epsilon(m_{Kp}, \Omega) dm_{Kp} d\Omega \\ &\propto \sum_j^{N_{\text{MC}}} w_j^{\text{MC}} |\mathcal{M}(m_{Kp j}, \Omega_j | \vec{\omega})|^2, \end{aligned} \quad (72)$$

where w_j^{MC} are the weights given to the simulated events to improve the agreement between data and simulations. They include particle identification weights obtained from calibration samples of $\Lambda \rightarrow p\pi^-$ and $D^0 \rightarrow K^-\pi^+$ as functions of momentum and pseudorapidity of

the protons and kaons. They also include a weight correcting the overall efficiency for the dependence on the charged track multiplicity of events, determined from the ratio of the background-subtracted data and the signal simulations. Imperfect description of the Λ_b^0 production kinematics in our simulation is corrected in a similar way via a weight that depends on the p and p_T of the Λ_b^0 baryon. The final weights are the ratio of the data and the simulations as a function of proton and kaon momenta.

In the cFit approach, candidates are not weighted ($W_i = 1$). The data that are fitted are restricted to be within a $\pm 2\sigma$ mass window around the Λ_b^0 mass peak, in the interval $5605.7 < m_{J/\psi p K} < 5635.8$ MeV. The background is represented explicitly in the fitted PDF, with the integrated background probability set to $\beta = 5.4\%$ as determined from the fit to the $J/\psi K^- p$ mass distribution,

$$\mathcal{P}(m_{Kp}, \Omega | \vec{\omega}) = (1 - \beta) \mathcal{P}_{\text{sig}}(m_{Kp}, \Omega | \vec{\omega}) + \beta \mathcal{P}_{\text{bkg}}(m_{Kp}, \Omega). \quad (73)$$

The 6-dimensional background parameterization $\mathcal{P}_{\text{bkg}}(m_{Kp}, \Omega)$ is developed using the background sample in which the Λ_b^0 candidate invariant mass is more than 5σ away from the peak, specifically within the intervals $5480.0 - 5583.2$ MeV and $5658.3 - 5760.0$ MeV. We minimize the negative log-likelihood defined as,

$$\begin{aligned} -2 \ln \mathcal{L}(\vec{\omega}) &= \\ &= -2 \sum_i \ln \left[(1 - \beta) \frac{|\mathcal{M}(m_{Kp\ i}, \Omega_i | \vec{\omega})|^2 \Phi(m_{Kp\ i}) \epsilon(m_{Kp\ i}, \Omega_i)}{I(\vec{\omega})} + \beta \frac{\mathcal{P}_{\text{bkg}}^u(m_{Kp\ i}, \Omega_i)}{I_{\text{bkg}}} \right] \\ &= -2 \sum_i \ln \left[|\mathcal{M}(m_{Kp\ i}, \Omega_i | \vec{\omega})|^2 + \frac{\beta I(\vec{\omega})}{(1 - \beta) I_{\text{bkg}}} \frac{\mathcal{P}_{\text{bkg}}^u(m_{Kp\ i}, \Omega_i)}{\Phi(m_{Kp\ i}) \epsilon(m_{Kp\ i}, \Omega_i)} \right] \\ &\quad + 2N \ln I(\vec{\omega}) + \text{constant}, \end{aligned} \quad (74)$$

where N is the number of candidates, and $\mathcal{P}_{\text{bkg}}^u(m_{Kp}, \Omega)$ is the unnormalized background density proportional to the density of sideband candidates, with its normalization determined by⁹

$$I_{\text{bkg}} \equiv \int \mathcal{P}_{\text{bkg}}^u(m_{Kp}) dm_{Kp} d\Omega \propto \sum_j w_j^{\text{MC}} \frac{\mathcal{P}_{\text{bkg}}^u(m_{Kp\ j}, \Omega_j)}{\Phi(m_{Kp\ j}) \epsilon(m_{Kp\ j}, \Omega_j)}. \quad (75)$$

The background term is then efficiency-corrected so it can be added to the efficiency-independent signal probability expressed by $|\mathcal{M}|^2$. This way the efficiency parametrization, $\epsilon(m_{Kp}, \Omega)$, influences only the background component which affects only a tiny part of the total PDF, while the efficiency corrections to the signal part enter Eq. (72).

The efficiency in the background term is assumed to factorize as

$$\epsilon(m_{Kp}, \Omega) = \epsilon_1(m_{Kp}, \cos \theta_A^*) \epsilon_2(\cos \theta_{\Lambda_b^0} | m_{Kp}) \epsilon_3(\cos \theta_{J/\psi} | m_{Kp}) \epsilon_4(\phi_K | m_{Kp}) \epsilon_5(\phi_\mu | m_{Kp}). \quad (76)$$

⁹Note that the distribution of MC events includes both the $\Phi(m_{Kp})$ and $\epsilon(m_{Kp}, \Omega)$ factors, which cancel their product in the numerator.

The $\epsilon_1(m_{Kp}, \cos \theta_\Lambda^*)$ term is obtained from a 2D histogram of the simulated events weighted by $1/(pq)$. A bi-cubic interpolation is used to interpolate between bin centers. The other terms are again built from 2D histograms, but with each bin divided by the number of simulated events in the corresponding m_{Kp} slice to remove the leading dependence on this mass, which is already taken into account in the first term. The leading variation of the efficiency is in the $\epsilon_1(m_{Kp}, \cos \theta_\Lambda^*)$ term which is visualized in the normal Dalitz variables ($m_{J/\psi p}^2, m_{Kp}^2$) in Fig. 18(a) instead of the “rectangular Dalitz plane” variables ($m_{Kp}, \cos \theta_\Lambda^*$) used to parameterize this variation.

The background PDF, $\mathcal{P}_{\text{bkg}}^u(m_{Kp}, \Omega)/\Phi(m_{Kp})$, is built using the same approach,

$$\frac{\mathcal{P}_{\text{bkg}}^u(m_{Kp}, \Omega)}{\Phi(m_{Kp})} = P_{\text{bkg1}}(m_{Kp}, \cos \theta_\Lambda^*) P_{\text{bkg2}}(\cos \theta_{\Lambda_b^0} | m_{Kp}) \\ \times P_{\text{bkg3}}(\cos \theta_{J/\psi} | m_{Kp}) P_{\text{bkg4}}(\phi_K | m_{Kp}) P_{\text{bkg5}}(\phi_\mu | m_{Kp}). \quad (77)$$

A visualization of $P_{\text{bkg1}}(m_{Kp}, \cos \theta_\Lambda^*)$ on the Dalitz plane is shown in Fig. 18(b).

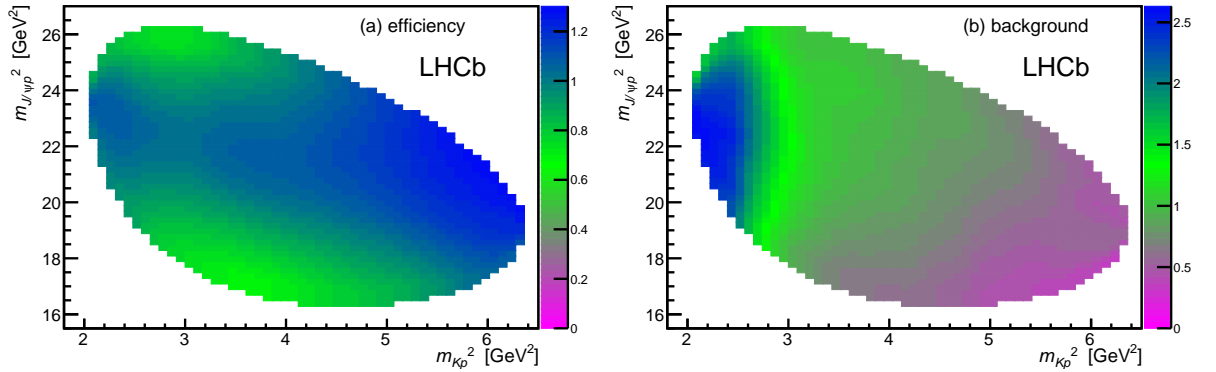


Figure 18: Parameterized dependence of (a) the relative signal efficiency and of (b) the background density on the Dalitz plane. The units of the relative efficiency and of the relative background density are arbitrary.

References

- [1] M. Gell-Mann, *A schematic model of baryons and mesons*, Phys. Lett. **8** (1964) 214.
- [2] R. L. Jaffe, *Multiquark hadrons. I. Phenomenology of $Q^2\bar{Q}^2$ mesons*, Phys. Rev. **D15** (1977) 267.
- [3] D. Strottman, *Multi-quark baryons and the MIT bag model*, Phys. Rev. **D20** (1979) 748.
- [4] H. J. Lipkin, *New possibilities for exotic hadrons: Anticharmed strange baryons*, Phys. Lett. **B195** (1987) 484.
- [5] K. H. Hicks, *On the conundrum of the pentaquark*, Eur. Phys. J. **H37** (2012) 1.
- [6] Belle collaboration, S. K. Choi *et al.*, *Observation of a resonance-like structure in the $\pi^\pm\psi'$ mass distribution in exclusive $B \rightarrow K\pi^\pm\psi'$ decays*, Phys. Rev. Lett. **100** (2008) 142001, [arXiv:0708.1790](#).
- [7] Belle collaboration, K. Chilikin *et al.*, *Experimental constraints on the spin and parity of the $Z(4430)^+$* , Phys. Rev. **D88** (2013) 074026, [arXiv:1306.4894](#).
- [8] LHCb collaboration, R. Aaij *et al.*, *Observation of the resonant character of the $Z(4430)^-$ state*, Phys. Rev. Lett. **112** (2014) 222002, [arXiv:1404.1903](#).
- [9] X.-Q. Li and X. Liu, *A possible global group structure for exotic states*, Eur. Phys. J. **C74** (2014) 3198, [arXiv:1409.3332](#).
- [10] LHCb collaboration, R. Aaij *et al.*, *Precision measurement of the ratio of the Λ_b^0 to \bar{B}^0 lifetimes*, Phys. Lett. **B734** (2014) 122, [arXiv:1402.6242](#); LHCb collaboration, R. Aaij *et al.*, *Precision measurement of the Λ_b^0 baryon lifetime*, Phys. Rev. Lett. **111** (2013) 102003, [arXiv:1307.2476](#).
- [11] Particle Data Group, K. A. Olive *et al.*, *Review of particle physics*, Chin. Phys. **C38** (2014) 090001.
- [12] LHCb collaboration, A. A. Alves Jr. *et al.*, *The LHCb detector at the LHC*, JINST **3** (2008) S08005.
- [13] R. Aaij *et al.*, *Performance of the LHCb Vertex Locator*, JINST **9** (2014) P09007, [arXiv:1405.7808](#).
- [14] R. Arink *et al.*, *Performance of the LHCb Outer Tracker*, JINST **9** (2014) P01002, [arXiv:1311.3893](#).
- [15] M. Adinolfi *et al.*, *Performance of the LHCb RICH detector at the LHC*, Eur. Phys. J. **C73** (2013) 2431, [arXiv:1211.6759](#).

- [16] A. A. Alves Jr. *et al.*, *Performance of the LHCb muon system*, JINST **8** (2013) P02022, [arXiv:1211.1346](#).
- [17] LHCb collaboration, R. Aaij *et al.*, *First observation of $B_s^0 \rightarrow J/\psi f_0(980)$ decays*, Phys. Lett. **B698** (2011) 115, [arXiv:1102.0206](#).
- [18] L. Breiman, J. H. Friedman, R. A. Olshen, and C. J. Stone, *Classification and regression trees*, Wadsworth international group, Belmont, California, USA, 1984; A. Hoecker *et al.*, *TMVA – Toolkit for multivariate data analysis*, [arXiv:physics/0703039](#).
- [19] T. Sjöstrand, S. Mrenna, and P. Skands, *PYTHIA 6.4 physics and manual*, JHEP **05** (2006) 026, [arXiv:hep-ph/0603175](#); T. Sjöstrand, S. Mrenna, and P. Skands, *A brief introduction to PYTHIA 8.1*, Comput. Phys. Commun. **178** (2008) 852, [arXiv:0710.3820](#).
- [20] I. Belyaev *et al.*, *Handling of the generation of primary events in Gauss, the LHCb simulation framework*, J. Phys. Conf. Ser. **331** (2011) 032047.
- [21] Geant4 collaboration, S. Agostinelli *et al.*, *Geant4: A simulation toolkit*, Nucl. Instrum. Meth. **A506** (2003) 250; Geant4 collaboration, J. Allison *et al.*, *Geant4 developments and applications*, IEEE Trans. Nucl. Sci. **53** (2006) 270.
- [22] M. Clemencic *et al.*, *The LHCb simulation application, Gauss: Design, evolution and experience*, Journal of Physics: Conference Series **331** (2011) 032023.
- [23] D. Martínez Santos and F. Dupertuis, *Mass distributions marginalized over per-event errors*, Nucl. Instrum. Meth. **A764** (2014) 150, [arXiv:1312.5000](#).
- [24] W. D. Hulsbergen, *Decay chain fitting with a Kalman filter*, Nucl. Instrum. Meth. **A552** (2005) 566, [arXiv:physics/0503191](#).
- [25] R. H. Dalitz, *On the analysis of τ -meson data and the nature of the τ -meson*, Phil. Mag. **44** (1953) 1068.
- [26] S. U. Chung, *Spin formalisms*, CERN-71-08; J. D. Richman, *An experimenter's guide to the helicity formalism*, CALT-68-1148; M. Jacob and G. C. Wick, *On the general theory of collisions for particles with spin*, Annals Phys. **7** (1959) 404.
- [27] F. Von Hippel and C. Quigg, *Centrifugal-barrier effects in resonance partial decay widths, shapes, and production amplitudes*, Phys. Rev. **D5** (1972) 624.
- [28] S. M. Flatté, *Coupled-channel analysis of the $\pi\eta$ and $K\bar{K}$ systems near $K\bar{K}$ threshold*, Phys. Lett. **B63** (1976) 224.
- [29] M. Pivk and F. R. Le Diberder, *sPlot: A statistical tool to unfold data distributions*, Nucl. Instrum. Meth. **A555** (2005) 356, [arXiv:physics/0402083](#).

- [30] F. James, *Statistical methods in experimental physics*, World Scientific Publishing, 2006.
- [31] J. F. Donoghue, E. Golowich, W. A. Ponce, and B. R. Holstein, *Analysis of $\Delta S=1$ nonleptonic weak decays and the $\Delta I=1/2$ rule*, Phys. Rev. **D21** (1980) 186.
- [32] LHCb collaboration, R. Aaij *et al.*, *Observation of overlapping spin-1 and spin-3 $\bar{D}^0 K^-$ resonances at mass 2.86 GeV/ c^2* , Phys. Rev. Lett. **113** (2014) 162001, [arXiv:1407.7574](#); LHCb collaboration, R. Aaij *et al.*, *Dalitz plot analysis of $B_s^0 \rightarrow \bar{D}^0 K^- \pi^+$ decays*, Phys. Rev. **D90** (2014) 072003, [arXiv:1407.7712](#).
- [33] R. L. Jaffe and F. Wilczek, *Diquarks and exotic spectroscopy*, Phys. Rev. Lett. **91** (2003) 232003, [arXiv:hep-ph/0307341](#).
- [34] A. Chandra, A. Bhattacharya, and B. Chakrabarti, *Heavy pentaquarks and doubly heavy baryons in quasiparticle approach*, Mod. Phys. Lett. **A27** (2012) 1250006.
- [35] M. Karliner and H. J. Lipkin, *A diquark - triquark model for the KN pentaquark*, Phys. Lett. **B575** (2003) 249, [arXiv:hep-ph/0402260](#).
- [36] J.-J. Wu, R. Molina, E. Oset, and B. S. Zou, *Prediction of narrow N^* and Λ^* resonances with hidden charm above 4 GeV*, Phys. Rev. Lett. **105** (2010) 232001, [arXiv:1007.0573](#).
- [37] M. B. Voloshin and L. B. Okun, *Hadron molecules and charmonium atom*, JETP Lett. **23** (1976) 333; A. De Rujula, H. Georgi, and S. L. Glashow, *Molecular charmonium: a new spectroscopy?*, Phys. Rev. Lett. **38** (1977) 317; N. A. Törnqvist, *Possible large deuteron-like meson meson states bound by pions*, Phys. Rev. Lett. **67** (1991) 556; N. A. Törnqvist, *From the deuteron to deusons, an analysis of deuteron-like meson meson bound states*, Z. Phys. **C61** (1994) 525, [arXiv:hep-ph/9310247](#); M. Karliner and J. L. Rosner, *New exotic meson and baryon resonances from doubly-heavy hadronic molecules*, [arXiv:1506.06386](#).
- [38] E. S. Swanson, *Cusps and exotic charmonia*, [arXiv:1504.07952](#).
- [39] E. S. Swanson, *Z_b and Z_c exotic states as coupled channel cusps*, Phys. Rev. **D91** (2015) 034009, [arXiv:1409.3291](#).
- [40] D. V. Bugg, *An explanation of Belle states $Z_b(10610)$ and $Z_b(10650)$* , Europhys. Lett. **96** (2011) 11002, [arXiv:1105.5492](#).
- [41] J. M. Blatt and V. F. Weisskopf, *Theoretical Nuclear Physics*, Springer-Verlag, 1979.
- [42] LHCb collaboration, R. Aaij *et al.*, *Measurements of the $\Lambda_b^0 \rightarrow J/\psi \Lambda$ decay amplitudes and the Λ_b^0 polarization in pp collisions at $\sqrt{s} = 7$ TeV*, Phys. Lett. **B724** (2013) 27, [arXiv:1302.5578](#).

- [43] Belle collaboration, R. Mizuk *et al.*, *Observation of two resonance-like structures in the $\pi^+\chi_{c1}$ mass distribution in exclusive $\bar{B}^0 \rightarrow K^-\pi^+\chi_{c1}$ decays*, Phys. Rev. **D78** (2008) 072004, [arXiv:0806.4098](#).
- [44] LHCb, R. Aaij *et al.*, *Precision measurement of CP violation in $B_s^0 \rightarrow J/\psi K^+K^-$ decays*, Phys. Rev. Lett. **114** (2015) 041801, [arXiv:1411.3104](#).

LHCb collaboration

R. Aaij³⁸, B. Adeva³⁷, M. Adinolfi⁴⁶, A. Affolder⁵², Z. Ajaltouni⁵, S. Akar⁶, J. Albrecht⁹, F. Alessio³⁸, M. Alexander⁵¹, S. Ali⁴¹, G. Alkhazov³⁰, P. Alvarez Cartelle⁵³, A.A. Alves Jr⁵⁷, S. Amato², S. Amerio²², Y. Amhis⁷, L. An³, L. Anderlini¹⁷, J. Anderson⁴⁰, G. Andreassi³⁹, M. Andreotti^{16,f}, J.E. Andrews⁵⁸, R.B. Appleby⁵⁴, O. Aquines Gutierrez¹⁰, F. Archilli³⁸, P. d'Argent¹¹, A. Artamonov³⁵, M. Artuso⁵⁹, E. Aslanides⁶, G. Auriemma^{25,m}, M. Baalouch⁵, S. Bachmann¹¹, J.J. Back⁴⁸, A. Badalov³⁶, C. Baesso⁶⁰, W. Baldini^{16,38}, R.J. Barlow⁵⁴, C. Barschel³⁸, S. Barsuk⁷, W. Barter³⁸, V. Batozskaya²⁸, V. Battista³⁹, A. Bay³⁹, L. Beaucourt⁴, J. Beddow⁵¹, F. Bedeschi²³, I. Bediaga¹, L.J. Bel⁴¹, V. Bellec³⁹, N. Belloli²⁰, I. Belyaev³¹, E. Ben-Haim⁸, G. Bencivenni¹⁸, S. Benson³⁸, J. Benton⁴⁶, A. Berezhnoy³², R. Bernet⁴⁰, A. Bertolin²², M.-O. Bettler³⁸, M. van Beuzekom⁴¹, A. Bien¹¹, S. Bifani⁴⁵, P. Billoir⁸, T. Bird⁵⁴, A. Birnkraut⁹, A. Bizzeti^{17,h}, T. Blake⁴⁸, F. Blanc³⁹, J. Blouw¹⁰, S. Blusk⁵⁹, V. Bocci²⁵, A. Bondar³⁴, N. Bondar^{30,38}, W. Bonivento¹⁵, S. Borghi⁵⁴, M. Borsato⁷, T.J.V. Bowcock⁵², E. Bowen⁴⁰, C. Bozzi¹⁶, S. Braun¹¹, M. Britsch¹⁰, T. Britton⁵⁹, J. Brodzicka⁵⁴, N.H. Brook⁴⁶, A. Bursche⁴⁰, J. Buytaert³⁸, S. Cadeddu¹⁵, R. Calabrese^{16,f}, M. Calvi^{20,j}, M. Calvo Gomez^{36,o}, P. Campana¹⁸, D. Campora Perez³⁸, L. Capriotti⁵⁴, A. Carbone^{14,d}, G. Carboni^{24,k}, R. Cardinale^{19,i}, A. Cardini¹⁵, P. Carniti²⁰, L. Carson⁵⁰, K. Carvalho Akiba^{2,38}, G. Casse⁵², L. Cassina^{20,j}, L. Castillo Garcia³⁸, M. Cattaneo³⁸, Ch. Cauet⁹, G. Cavallero¹⁹, R. Cenci^{23,s}, M. Charles⁸, Ph. Charpentier³⁸, M. Chefdeville⁴, S. Chen⁵⁴, S.-F. Cheung⁵⁵, N. Chiapolini⁴⁰, M. Chrzaszcz⁴⁰, X. Cid Vidal³⁸, G. Ciezarek⁴¹, P.E.L. Clarke⁵⁰, M. Clemencic³⁸, H.V. Cliff⁴⁷, J. Closier³⁸, V. Coco³⁸, J. Cogan⁶, E. Cogneras⁵, V. Cogoni^{15,e}, L. Cojocariu²⁹, G. Collazuol²², P. Collins³⁸, A. Comerma-Montells¹¹, A. Contu^{15,38}, A. Cook⁴⁶, M. Coombes⁴⁶, S. Coquereau⁸, G. Corti³⁸, M. Corvo^{16,f}, B. Couturier³⁸, G.A. Cowan⁵⁰, D.C. Craik⁴⁸, A. Crocombe⁴⁸, M. Cruz Torres⁶⁰, S. Cunliffe⁵³, R. Currie⁵³, C. D'Ambrosio³⁸, E. Dall'Occo⁴¹, J. Dalseno⁴⁶, P.N.Y. David⁴¹, A. Davis⁵⁷, K. De Bruyn⁴¹, S. De Capua⁵⁴, M. De Cian¹¹, J.M. De Miranda¹, L. De Paula², P. De Simone¹⁸, C.-T. Dean⁵¹, D. Decamp⁴, M. Deckenhoff⁹, L. Del Buono⁸, N. Déléage⁴, M. Demmer⁹, D. Derkach⁵⁵, O. Deschamps⁵, F. Dettori³⁸, B. Dey²¹, A. Di Canto³⁸, F. Di Ruscio²⁴, H. Dijkstra³⁸, S. Donleavy⁵², F. Dordei¹¹, M. Dorigo³⁹, A. Dosil Suárez³⁷, D. Dossett⁴⁸, A. Dovbnya⁴³, K. Dreimanis⁵², L. Dufour⁴¹, G. Dujany⁵⁴, F. Dupertuis³⁹, P. Durante³⁸, R. Dzhelyadin³⁵, A. Dziurda²⁶, A. Dzyuba³⁰, S. Easo^{49,38}, U. Egede⁵³, V. Egorychev³¹, S. Eidelman³⁴, S. Eisenhardt⁵⁰, U. Eitschberger⁹, R. Ekelhof⁹, L. Eklund⁵¹, I. El Rifai⁵, Ch. Elsasser⁴⁰, S. Ely⁵⁹, S. Esen¹¹, H.M. Evans⁴⁷, T. Evans⁵⁵, A. Falabella¹⁴, C. Färber³⁸, N. Farley⁴⁵, S. Farry⁵², R. Fay⁵², D. Ferguson⁵⁰, V. Fernandez Albor³⁷, F. Ferrari¹⁴, F. Ferreira Rodrigues¹, M. Ferro-Luzzi³⁸, S. Filippov³³, M. Fiore^{16,38,f}, M. Fiorini^{16,f}, M. Firlej²⁷, C. Fitzpatrick³⁹, T. Fiutowski²⁷, K. Fohl³⁸, P. Fol⁵³, M. Fontana¹⁵, F. Fontanelli^{19,i}, R. Forty³⁸, O. Francisco², M. Frank³⁸, C. Frei³⁸, M. Frosini¹⁷, J. Fu²¹, E. Furfaro^{24,k}, A. Gallas Torreira³⁷, D. Galli^{14,d}, S. Gallorini^{22,38}, S. Gambetta⁵⁰, M. Gandelman², P. Gandini⁵⁵, Y. Gao³, J. García Pardiñas³⁷, J. Garra Tico⁴⁷, L. Garrido³⁶, D. Gascon³⁶, C. Gaspar³⁸, R. Gauld⁵⁵, L. Gavardi⁹, G. Gazzoni⁵, A. Geraci^{21,u}, D. Gerick¹¹, E. Gersabeck¹¹, M. Gersabeck⁵⁴, T. Gershon⁴⁸, Ph. Ghez⁴, A. Gianelle²², S. Giani³⁹, V. Gibson⁴⁷, O. G. Girard³⁹, L. Giubega²⁹, V.V. Gligorov³⁸, C. Göbel⁶⁰, D. Golubkov³¹, A. Golutvin^{53,31,38}, A. Gomes^{1,a}, C. Gotti^{20,j}, M. Grabalosa Gándara⁵, R. Graciani Diaz³⁶, L.A. Granado Cardoso³⁸, E. Graugés³⁶, E. Graverini⁴⁰, G. Graziani¹⁷, A. Grecu²⁹, E. Greening⁵⁵, S. Gregson⁴⁷, P. Griffith⁴⁵, L. Grillo¹¹, O. Grünberg⁶³, B. Gui⁵⁹, E. Gushchin³³, Yu. Guz^{35,38}, T. Gys³⁸, T. Hadavizadeh⁵⁵, C. Hadjivasiliou⁵⁹, G. Haefeli³⁹, C. Haen³⁸,

S.C. Haines⁴⁷, S. Hall⁵³, B. Hamilton⁵⁸, X. Han¹¹, S. Hansmann-Menzemer¹¹, N. Harnew⁵⁵,
 S.T. Harnew⁴⁶, J. Harrison⁵⁴, J. He³⁸, T. Head³⁹, V. Heijne⁴¹, K. Hennessy⁵², P. Henrard⁵,
 L. Henry⁸, J.A. Hernando Morata³⁷, E. van Herwijnen³⁸, M. Heß⁶³, A. Hicheur², D. Hill⁵⁵,
 M. Hoballah⁵, C. Hombach⁵⁴, W. Hulsbergen⁴¹, T. Humair⁵³, N. Hussain⁵⁵, D. Hutchcroft⁵²,
 D. Hynds⁵¹, M. Idzik²⁷, P. Ilten⁵⁶, R. Jacobsson³⁸, A. Jaeger¹¹, J. Jalocha⁵⁵, E. Jans⁴¹,
 A. Jawahery⁵⁸, F. Jing³, M. John⁵⁵, D. Johnson³⁸, C.R. Jones⁴⁷, C. Joram³⁸, B. Jost³⁸,
 N. Jurik⁵⁹, S. Kandybei⁴³, W. Kanso⁶, M. Karacson³⁸, T.M. Karbach^{38,†}, S. Karodia⁵¹,
 M. Kecke¹¹, M. Kelsey⁵⁹, I.R. Kenyon⁴⁵, M. Kenzie³⁸, T. Ketel⁴², B. Khanji^{20,38,j},
 C. Khurewathanakul³⁹, S. Klaver⁵⁴, K. Klimaszewski²⁸, O. Kochebina⁷, M. Kolpin¹¹,
 I. Komarov³⁹, R.F. Koopman⁴², P. Koppenburg^{41,38}, M. Kozeiha⁵, L. Kravchuk³³, K. Kreplin¹¹,
 M. Kreps⁴⁸, G. Krocker¹¹, P. Krokovny³⁴, F. Kruse⁹, W. Krzemien²⁸, W. Kucewicz^{26,n},
 M. Kucharczyk²⁶, V. Kudryavtsev³⁴, A. K. Kuonen³⁹, K. Kurek²⁸, T. Kvaratskheliya³¹,
 D. Lacarrere³⁸, G. Lafferty⁵⁴, A. Lai¹⁵, D. Lambert⁵⁰, G. Lanfranchi¹⁸, C. Langenbruch⁴⁸,
 B. Langhans³⁸, T. Latham⁴⁸, C. Lazzeroni⁴⁵, R. Le Gac⁶, J. van Leerdam⁴¹, J.-P. Lees⁴,
 R. Lefevre⁵, A. Leflat^{32,38}, J. Lefrançois⁷, O. Leroy⁶, T. Lesiak²⁶, B. Leverington¹¹, Y. Li⁷,
 T. Likhomanenko^{65,64}, M. Liles⁵², R. Lindner³⁸, C. Linn³⁸, F. Lionetto⁴⁰, B. Liu¹⁵, X. Liu³,
 D. Loh⁴⁸, I. Longstaff⁵¹, J.H. Lopes², D. Lucchesi^{22,q}, M. Lucio Martinez³⁷, H. Luo⁵⁰,
 A. Lupato²², E. Luppi^{16,f}, O. Lupton⁵⁵, N. Lusardi²¹, A. Lusiani²³, F. Machefert⁷, F. Maciuc²⁹,
 O. Maev³⁰, K. Maguire⁵⁴, S. Malde⁵⁵, A. Malinin⁶⁴, G. Manca⁷, G. Mancinelli⁶, P. Manning⁵⁹,
 A. Mapelli³⁸, J. Maratas⁵, J.F. Marchand⁴, U. Marconi¹⁴, C. Marin Benito³⁶, P. Marino^{23,38,s},
 J. Marks¹¹, G. Martellotti²⁵, M. Martin⁶, M. Martinelli³⁹, D. Martinez Santos³⁷,
 F. Martinez Vidal⁶⁶, D. Martins Tostes², A. Massafferri¹, R. Matev³⁸, A. Mathad⁴⁸, Z. Mathe³⁸,
 C. Matteuzzi²⁰, A. Mauri⁴⁰, B. Maurin³⁹, A. Mazurov⁴⁵, M. McCann⁵³, J. McCarthy⁴⁵,
 A. McNab⁵⁴, R. McNulty¹², B. Meadows⁵⁷, F. Meier⁹, M. Meissner¹¹, D. Melnychuk²⁸,
 M. Merk⁴¹, D.A. Milanes⁶², M.-N. Minard⁴, D.S. Mitzel¹¹, J. Molina Rodriguez⁶⁰,
 I.A. Monroy⁶², S. Monteil⁵, M. Morandin²², P. Morawski²⁷, A. Mordà⁶, M.J. Morello^{23,s},
 J. Moron²⁷, A.B. Morris⁵⁰, R. Mountain⁵⁹, F. Muheim⁵⁰, J. Müller⁹, K. Müller⁴⁰, V. Müller⁹,
 M. Mussini¹⁴, B. Muster³⁹, P. Naik⁴⁶, T. Nakada³⁹, R. Nandakumar⁴⁹, A. Nandi⁵⁵, I. Nasteva²,
 M. Needham⁵⁰, N. Neri²¹, S. Neubert¹¹, N. Neufeld³⁸, M. Neuner¹¹, A.D. Nguyen³⁹,
 T.D. Nguyen³⁹, C. Nguyen-Mau^{39,p}, V. Niess⁵, R. Niet⁹, N. Nikitin³², T. Nikodem¹¹, D. Ninci²³,
 A. Novoselov³⁵, D.P. O’Hanlon⁴⁸, A. Oblakowska-Mucha²⁷, V. Obraztsov³⁵, S. Ogilvy⁵¹,
 O. Okhrimenko⁴⁴, R. Oldeman^{15,e}, C.J.G. Onderwater⁶⁷, B. Osorio Rodrigues¹,
 J.M. Otalora Goicochea², A. Otto³⁸, P. Owen⁵³, A. Oyanguren⁶⁶, A. Palano^{13,c}, F. Palombo^{21,t},
 M. Palutan¹⁸, J. Panman³⁸, A. Papanestis⁴⁹, M. Pappagallo⁵¹, L.L. Pappalardo^{16,f},
 C. Pappenheimer⁵⁷, C. Parkes⁵⁴, G. Passaleva¹⁷, G.D. Patel⁵², M. Patel⁵³, C. Patrignani^{19,i},
 A. Pearce^{54,49}, A. Pellegrino⁴¹, G. Penso^{25,l}, M. Pepe Altarelli³⁸, S. Perazzini^{14,d}, P. Perret⁵,
 L. Pescatore⁴⁵, K. Petridis⁴⁶, A. Petrolini^{19,i}, M. Petruzzo²¹, E. Picatoste Olloqui³⁶,
 B. Pietrzyk⁴, T. Pilarš⁴⁸, D. Pinci²⁵, A. Pistone¹⁹, A. Piucci¹¹, S. Playfer⁵⁰, M. Plo Casasus³⁷,
 T. Poikela³⁸, F. Polci⁸, A. Poluektov^{48,34}, I. Polyakov³¹, E. Polycarpo², A. Popov³⁵,
 D. Popov^{10,38}, B. Popovici²⁹, C. Potterat², E. Price⁴⁶, J.D. Price⁵², J. Prisciandaro³⁹,
 A. Pritchard⁵², C. Prouve⁴⁶, V. Pugatch⁴⁴, A. Puig Navarro³⁹, G. Punzi^{23,r}, W. Qian⁴,
 R. Quagliani^{7,46}, B. Rachwal²⁶, J.H. Rademacker⁴⁶, M. Rama²³, M.S. Rangel², I. Raniuk⁴³,
 N. Rauschmayr³⁸, G. Raven⁴², F. Redi⁵³, S. Reichert⁵⁴, M.M. Reid⁴⁸, A.C. dos Reis¹,
 S. Ricciardi⁴⁹, S. Richards⁴⁶, M. Rihl³⁸, K. Rinnert⁵², V. Rives Molina³⁶, P. Robbe^{7,38},
 A.B. Rodrigues¹, E. Rodrigues⁵⁴, J.A. Rodriguez Lopez⁶², P. Rodriguez Perez⁵⁴, S. Roiser³⁸,
 V. Romanovsky³⁵, A. Romero Vidal³⁷, J. W. Ronayne¹², M. Rotondo²², J. Rouvinet³⁹, T. Ruf³⁸,

P. Ruiz Valls⁶⁶, J.J. Saborido Silva³⁷, N. Sagidova³⁰, P. Sail⁵¹, B. Saitta^{15,e},
V. Salustino Guimaraes², C. Sanchez Mayordomo⁶⁶, B. Sanmartin Sedes³⁷, R. Santacesaria²⁵,
C. Santamarina Rios³⁷, M. Santimaria¹⁸, E. Santovetti^{24,k}, A. Sarti^{18,l}, C. Satriano^{25,m},
A. Satta²⁴, D.M. Saunders⁴⁶, D. Savrina^{31,32}, M. Schiller³⁸, H. Schindler³⁸, M. Schlupp⁹,
M. Schmelling¹⁰, T. Schmelzer⁹, B. Schmidt³⁸, O. Schneider³⁹, A. Schopper³⁸, M. Schubiger³⁹,
M.-H. Schune⁷, R. Schwemmer³⁸, B. Sciascia¹⁸, A. Sciubba^{25,l}, A. Semennikov³¹, N. Serra⁴⁰,
J. Serrano⁶, L. Sestini²², P. Seyfert²⁰, M. Shapkin³⁵, I. Shapoval^{16,43,f}, Y. Shcheglov³⁰,
T. Shears⁵², L. Shekhtman³⁴, V. Shevchenko⁶⁴, A. Shires⁹, B.G. Siddi¹⁶, R. Silva Coutinho⁴⁸,
G. Simi²², M. Sirendi⁴⁷, N. Skidmore⁴⁶, I. Skillicorn⁵¹, T. Skwarnicki⁵⁹, E. Smith^{55,49},
E. Smith⁵³, I. T. Smith⁵⁰, J. Smith⁴⁷, M. Smith⁵⁴, H. Snoek⁴¹, M.D. Sokoloff^{57,38}, F.J.P. Soler⁵¹,
F. Soomro³⁹, D. Souza⁴⁶, B. Souza De Paula², B. Spaan⁹, P. Spradlin⁵¹, S. Sridharan³⁸,
F. Stagni³⁸, M. Stahl¹¹, S. Stahl³⁸, S. Stefkova⁵³, O. Steinkamp⁴⁰, O. Stenyakin³⁵,
S. Stevenson⁵⁵, S. Stoica²⁹, S. Stone⁵⁹, B. Storaci⁴⁰, S. Stracka^{23,s}, M. Straticiu²⁹,
U. Straumann⁴⁰, L. Sun⁵⁷, W. Sutcliffe⁵³, K. Swientek²⁷, S. Swientek⁹, V. Syropoulos⁴²,
M. Szczekowski²⁸, P. Szczypka^{39,38}, T. Szumlak²⁷, S. T'Jampens⁴, A. Tayduganov⁶,
T. Tekampe⁹, M. Teklishyn⁷, G. Tellarini^{16,f}, F. Teubert³⁸, C. Thomas⁵⁵, E. Thomas³⁸,
J. van Tilburg⁴¹, V. Tisserand⁴, M. Tobin³⁹, J. Todd⁵⁷, S. Tolk⁴², L. Tomassetti^{16,f},
D. Tonelli³⁸, S. Topp-Joergensen⁵⁵, N. Torr⁵⁵, E. Tournefier⁴, S. Tourneur³⁹, K. Trabelsi³⁹,
M.T. Tran³⁹, M. Tresch⁴⁰, A. Trisovic³⁸, A. Tsaregorodtsev⁶, P. Tsopelas⁴¹, N. Tuning^{41,38},
A. Ukleja²⁸, A. Ustyuzhanin^{65,64}, U. Uwer¹¹, C. Vacca^{15,e}, V. Vagnoni¹⁴, G. Valenti¹⁴,
A. Vallier⁷, R. Vazquez Gomez¹⁸, P. Vazquez Regueiro³⁷, C. Vázquez Sierra³⁷, S. Vecchi¹⁶,
J.J. Velthuis⁴⁶, M. Veltri^{17,g}, G. Veneziano³⁹, M. Vesterinen¹¹, B. Viaud⁷, D. Vieira²,
M. Vieites Diaz³⁷, X. Vilasis-Cardona^{36,o}, A. Vollhardt⁴⁰, D. Volyanskyy¹⁰, D. Voong⁴⁶,
A. Vorobyev³⁰, V. Vorobyev³⁴, C. Voß⁶³, J.A. de Vries⁴¹, R. Waldi⁶³, C. Wallace⁴⁸, R. Wallace¹²,
J. Walsh²³, S. Wandernoth¹¹, J. Wang⁵⁹, D.R. Ward⁴⁷, N.K. Watson⁴⁵, D. Websdale⁵³,
A. Weiden⁴⁰, M. Whitehead⁴⁸, G. Wilkinson^{55,38}, M. Wilkinson⁵⁹, M. Williams³⁸,
M.P. Williams⁴⁵, M. Williams⁵⁶, T. Williams⁴⁵, F.F. Wilson⁴⁹, J. Wimberley⁵⁸, J. Wishahi⁹,
W. Wislicki²⁸, M. Witek²⁶, G. Wormser⁷, S.A. Wotton⁴⁷, S. Wright⁴⁷, K. Wyllie³⁸, Y. Xie⁶¹,
Z. Xu³⁹, Z. Yang³, J. Yu⁶¹, X. Yuan³⁴, O. Yushchenko³⁵, M. Zangoli¹⁴, M. Zavertyaev^{10,b},
L. Zhang³, Y. Zhang³, A. Zhelezov¹¹, A. Zhokhov³¹, L. Zhong³, S. Zucchelli¹⁴.

¹ Centro Brasileiro de Pesquisas Físicas (CBPF), Rio de Janeiro, Brazil

² Universidade Federal do Rio de Janeiro (UFRJ), Rio de Janeiro, Brazil

³ Center for High Energy Physics, Tsinghua University, Beijing, China

⁴ LAPP, Université Savoie Mont-Blanc, CNRS/IN2P3, Annecy-Le-Vieux, France

⁵ Clermont Université, Université Blaise Pascal, CNRS/IN2P3, LPC, Clermont-Ferrand, France

⁶ CPPM, Aix-Marseille Université, CNRS/IN2P3, Marseille, France

⁷ LAL, Université Paris-Sud, CNRS/IN2P3, Orsay, France

⁸ LPNHE, Université Pierre et Marie Curie, Université Paris Diderot, CNRS/IN2P3, Paris, France

⁹ Fakultät Physik, Technische Universität Dortmund, Dortmund, Germany

¹⁰ Max-Planck-Institut für Kernphysik (MPIK), Heidelberg, Germany

¹¹ Physikalisches Institut, Ruprecht-Karls-Universität Heidelberg, Heidelberg, Germany

¹² School of Physics, University College Dublin, Dublin, Ireland

¹³ Sezione INFN di Bari, Bari, Italy

¹⁴ Sezione INFN di Bologna, Bologna, Italy

¹⁵ Sezione INFN di Cagliari, Cagliari, Italy

¹⁶ Sezione INFN di Ferrara, Ferrara, Italy

¹⁷ Sezione INFN di Firenze, Firenze, Italy

- ¹⁸ *Laboratori Nazionali dell'INFN di Frascati, Frascati, Italy*
- ¹⁹ *Sezione INFN di Genova, Genova, Italy*
- ²⁰ *Sezione INFN di Milano Bicocca, Milano, Italy*
- ²¹ *Sezione INFN di Milano, Milano, Italy*
- ²² *Sezione INFN di Padova, Padova, Italy*
- ²³ *Sezione INFN di Pisa, Pisa, Italy*
- ²⁴ *Sezione INFN di Roma Tor Vergata, Roma, Italy*
- ²⁵ *Sezione INFN di Roma La Sapienza, Roma, Italy*
- ²⁶ *Henryk Niewodniczanski Institute of Nuclear Physics Polish Academy of Sciences, Kraków, Poland*
- ²⁷ *AGH - University of Science and Technology, Faculty of Physics and Applied Computer Science, Kraków, Poland*
- ²⁸ *National Center for Nuclear Research (NCBJ), Warsaw, Poland*
- ²⁹ *Horia Hulubei National Institute of Physics and Nuclear Engineering, Bucharest-Magurele, Romania*
- ³⁰ *Petersburg Nuclear Physics Institute (PNPI), Gatchina, Russia*
- ³¹ *Institute of Theoretical and Experimental Physics (ITEP), Moscow, Russia*
- ³² *Institute of Nuclear Physics, Moscow State University (SINP MSU), Moscow, Russia*
- ³³ *Institute for Nuclear Research of the Russian Academy of Sciences (INR RAN), Moscow, Russia*
- ³⁴ *Budker Institute of Nuclear Physics (SB RAS) and Novosibirsk State University, Novosibirsk, Russia*
- ³⁵ *Institute for High Energy Physics (IHEP), Protvino, Russia*
- ³⁶ *Universitat de Barcelona, Barcelona, Spain*
- ³⁷ *Universidad de Santiago de Compostela, Santiago de Compostela, Spain*
- ³⁸ *European Organization for Nuclear Research (CERN), Geneva, Switzerland*
- ³⁹ *Ecole Polytechnique Fédérale de Lausanne (EPFL), Lausanne, Switzerland*
- ⁴⁰ *Physik-Institut, Universität Zürich, Zürich, Switzerland*
- ⁴¹ *Nikhef National Institute for Subatomic Physics, Amsterdam, The Netherlands*
- ⁴² *Nikhef National Institute for Subatomic Physics and VU University Amsterdam, Amsterdam, The Netherlands*
- ⁴³ *NSC Kharkiv Institute of Physics and Technology (NSC KIPT), Kharkiv, Ukraine*
- ⁴⁴ *Institute for Nuclear Research of the National Academy of Sciences (KINR), Kyiv, Ukraine*
- ⁴⁵ *University of Birmingham, Birmingham, United Kingdom*
- ⁴⁶ *H.H. Wills Physics Laboratory, University of Bristol, Bristol, United Kingdom*
- ⁴⁷ *Cavendish Laboratory, University of Cambridge, Cambridge, United Kingdom*
- ⁴⁸ *Department of Physics, University of Warwick, Coventry, United Kingdom*
- ⁴⁹ *STFC Rutherford Appleton Laboratory, Didcot, United Kingdom*
- ⁵⁰ *School of Physics and Astronomy, University of Edinburgh, Edinburgh, United Kingdom*
- ⁵¹ *School of Physics and Astronomy, University of Glasgow, Glasgow, United Kingdom*
- ⁵² *Oliver Lodge Laboratory, University of Liverpool, Liverpool, United Kingdom*
- ⁵³ *Imperial College London, London, United Kingdom*
- ⁵⁴ *School of Physics and Astronomy, University of Manchester, Manchester, United Kingdom*
- ⁵⁵ *Department of Physics, University of Oxford, Oxford, United Kingdom*
- ⁵⁶ *Massachusetts Institute of Technology, Cambridge, MA, United States*
- ⁵⁷ *University of Cincinnati, Cincinnati, OH, United States*
- ⁵⁸ *University of Maryland, College Park, MD, United States*
- ⁵⁹ *Syracuse University, Syracuse, NY, United States*
- ⁶⁰ *Pontifícia Universidade Católica do Rio de Janeiro (PUC-Rio), Rio de Janeiro, Brazil, associated to ²*
- ⁶¹ *Institute of Particle Physics, Central China Normal University, Wuhan, Hubei, China, associated to ³*
- ⁶² *Departamento de Física, Universidad Nacional de Colombia, Bogota, Colombia, associated to ⁸*
- ⁶³ *Institut für Physik, Universität Rostock, Rostock, Germany, associated to ¹¹*
- ⁶⁴ *National Research Centre Kurchatov Institute, Moscow, Russia, associated to ³¹*
- ⁶⁵ *Yandex School of Data Analysis, Moscow, Russia, associated to ³¹*
- ⁶⁶ *Instituto de Física Corpuscular (IFIC), Universitat de Valencia-CSIC, Valencia, Spain, associated to ³⁶*
- ⁶⁷ *Van Swinderen Institute, University of Groningen, Groningen, The Netherlands, associated to ⁴¹*

- ^a *Universidade Federal do Triângulo Mineiro (UFMT), Uberaba-MG, Brazil*
- ^b *P.N. Lebedev Physical Institute, Russian Academy of Science (LPI RAS), Moscow, Russia*
- ^c *Università di Bari, Bari, Italy*
- ^d *Università di Bologna, Bologna, Italy*
- ^e *Università di Cagliari, Cagliari, Italy*
- ^f *Università di Ferrara, Ferrara, Italy*
- ^g *Università di Urbino, Urbino, Italy*
- ^h *Università di Modena e Reggio Emilia, Modena, Italy*
- ⁱ *Università di Genova, Genova, Italy*
- ^j *Università di Milano Bicocca, Milano, Italy*
- ^k *Università di Roma Tor Vergata, Roma, Italy*
- ^l *Università di Roma La Sapienza, Roma, Italy*
- ^m *Università della Basilicata, Potenza, Italy*
- ⁿ *AGH - University of Science and Technology, Faculty of Computer Science, Electronics and Telecommunications, Kraków, Poland*
- ^o *LIFAELS, La Salle, Universitat Ramon Llull, Barcelona, Spain*
- ^p *Hanoi University of Science, Hanoi, Viet Nam*
- ^q *Università di Padova, Padova, Italy*
- ^r *Università di Pisa, Pisa, Italy*
- ^s *Scuola Normale Superiore, Pisa, Italy*
- ^t *Università degli Studi di Milano, Milano, Italy*
- ^u *Politecnico di Milano, Milano, Italy*
- [†] *Deceased*